Published online 25 July 2022

Nucleic Acids Research, 2022, Vol. 50, No. 14 ***8041–8059***
https://doi.org/10.1093/nar/gkac621

R-loop-induced irreparable DNA damage evades checkpoint detection in the *C. elegans* germline

Tara Hicks, Emily Koury, Caleb McCabe, Cameron Williams, Caroline Crahan and Sarit Smolikove*

Department of Biology, The University of Iowa, IA City, IA 52242, USA

Received February 10, 2022; Revised June 28, 2022; Editorial Decision June 30, 2022; Accepted July 18, 2022

ABSTRACT

Accumulation of DNA–RNA hybrids in the form of R-loops can result in replication–transcription conflict that leads to the formation of DNA double strand breaks (DSBs). Using null mutants for the two *Caenorhabditis elegans* genes encoding for RNaseH1 and RNaseH2, we identify novel effects of R-loop accumulation in the germline. R-loop accumulation leads, as expected, to replication stress, followed by the formation of DSBs. A subset of these DSBs are irreparable. However, unlike irreparable DSBs generated in other systems, which trigger permanent cell cycle arrest, germline irreparable DSBs are propagated to oocytes. Despite DNA damage checkpoint activation in the stem cell niche, the signaling cannot be sustained and nuclei with irreparable DNA damage progress into meiosis. Moreover, unlike other forms of DNA damage that increase germline apoptosis, R-loop-generated DSBs remain undetected by the apoptotic checkpoint. This coincides with attenuation of ATM/ATR signaling in mid-to-late meiotic prophase I. These data altogether indicate that in the germline, DSBs that are generated by R-loops can lead to irreparable DSBs that evade cellular machineries designed for damage recognition. These studies implicate germline R-loops as an especially dangerous driver of germline mutagenesis.

INTRODUCTION

Due to the unwinding of DNA required for polymerase access during transcription, torsional stress is incurred which can result in the formation of anomalous structures like R-loops. R-loops are three-stranded nucleic acid structures composed of a DNA–RNA hybrid between the nascent exiting RNA and one of the displaced genomic single-stranded DNA (ssDNA) (1). Typically, the R-loop moiety arises when the newly-transcribed RNA invades the genomic DNA behind RNA polymerase forming the aforementioned long DNA–RNA hybrid and leaves the remaining ssDNA unable to rehybridize. This structure adopts a particularly stable conformation which requires enzymatic action to resolve back to the native double helix. R-loops are required for various cell physiological processes such as immunoglobulin class switching, termination of transcription, replication of mitochondrial DNA, and gene expression regulation. Misregulation and accumulation of R-loops can also have pathological effects on genome integrity in events where R-loops promote collision between the replisome and transcriptome. Halting of DNA replication has been shown to lead to the formation of DNA double strand breaks (DSBs), which in some cases stem from the cleavage of the replication fork by structure-specific nucleases (1,2). DSBs are among the most mutagenic and dangerous types of DNA lesions; a single DSB can result in cell lethality and/or genome instability. As such, the overaccumulation of R-loops in a cell represent a genomic threat. To prevent this kind of disastrous consequence, the cell employs various redundant mechanisms, one of which involves RNaseH enzymes which are responsible for degrading the nascent RNA strand of the R-loop (1,3,4).

While our understanding of R-loops within somatic cells is well-documented, the effect of R-loop formation on DSB repair in the germline is poorly understood. Thus, elucidating the mechanisms involved in repair of DNA damage formed by R-loops is important, since errors in DSB repair will lead to inheritance of genomic instability in the offspring. Moreover, the regulation of DNA damage repair is unique in meiotic cells as DSBs are induced, and thus form more frequently in meiotic germline nuclei than in any other phase of the cell cycle (5,6). The formation of DSBs within meiosis is a programmed event catalyzed by a topoisomerase-like complex involving Spo11 and is required for the formation of crossovers and faithful segregation of chromosomes into the gametes (7). Perturbed meiosis therefore can lead to aneuploidy and heritable mutagenesis. To prevent these effects, meiotic DSB repair is tightly regulated and preferentially channels breaks toward the

*To whom correspondence should be addressed. Tel: +1 319 335 1977; Email: sarit-smolikove@uiowa.edu
Present address: Sarit Smolikove, Department of Biology, The University of Iowa, Iowa City, IA 52242, USA.

© The Author(s) 2022. Published by Oxford University Press on behalf of Nucleic Acids Research.
This is an Open Access article distributed under the terms of the Creative Commons Attribution-NonCommercial License (http://creativecommons.org/licenses/by-nc/4.0/), which permits non-commercial re-use, distribution, and reproduction in any medium, provided the original work is properly cited. For commercial re-use, please contact journals.permissions@oup.com

homologous recombination (HR) pathway which ensures mostly error-free repair from the homologous template (8). In the *Caenorhabditis elegans* germline, DSBs associated with replication stress in germline stem cells can elicit temporary cell cycle arrest in the stem cell niche and apoptosis in meiotic prophase I (9). However, unrepaired DSBs can proceed into meiosis where nuclei containing persistent damage is eliminated by apoptosis. In some cases, when HR is abrogated and DSBs can only be repaired by error-prone DSB repair pathways oocytes showing genomic instability can form and proceed to fertilization (9–11). However, in germ cells proficient for HR, apoptosis can eliminate damaged nuclei, maintaining genomic stability.

The effect of R-loop-induced DSB formation on the meiotic repair network and consequently proper gamete formation varies among models and organisms, preventing a full understanding of the molecular mechanisms involved in repair of R-loop-induced DSBs within the meiotic environment. For example, mutants of the THO complex, an mRNP biogenesis factor, accumulate R-loop-induced DSBs in both *S. cerevisiae* and *C. elegans*. In *C. elegans thoc-2* mutants, DNA damage originates within germline stem cells and this damage persists into early meiotic prophase I (12). Unfortunately, the pleiotropic phenotypes arising as the result of loss of the THO complex arrest meiotic prophase before its completion (12), hindering the ability to study meiotic DSB repair in this background. Similar phenotypes have been observed in mice deficient in the transcription regulator Senataxin (13). *C. elegans* mutants deficient in H3K9me2/me3 deposition factors also experience R-loop accumulation as a result of unprogrammed transcription, but these effects are locus-specific (14,15). Unlike THO complex mutants, *met-2;set-25* mutants show mild and temperature-dependent effects on embryonic viability (14). Most importantly, *met-2;set-25* mutants show no accumulation of DNA damage in oocytes, but exhibit an increase in apoptosis, suggesting that checkpoint activation eliminates most of the damaged oocytes (14). Because R-loops arise as a result of unprogrammed transcription in this background, meiotic outcomes do not reflect the accumulation of R-loops at sites where they would naturally form (i.e. highly-transcribed regions). In yeast, a decrease or increase in R-loops is associated with reduced crossovers, but no such effect was observed in metazoan systems (16).

To fully understand the impact of R-loop formation on the germline, we generated a *C. elegans* strain which is deficient in the RNaseH enzymes RNH-1 and RNH-2. These RNaseH members have been shown to act redundantly in the dissolution of R-loops in yeast (16,17). As expected, we found that the R-loops which accumulate in RNaseH mutants lead to an increase in DNA damage. As a result, RNaseH mutants were able to complete meiosis and lay eggs, but exhibited an increase in genomic instability. We show that this is attributed to an inability to properly activate the DNA damage checkpoints both in the stem cell niche and in the meiotic germline. We posit that R-loop-induced DSBs that are irreparable, unlike other forms of DSBs, fail to persistently activate the DNA damage checkpoints. This adaptation to DNA damage leads to a previously undescribed threat that R-loops pose to genome integrity and the faithful passage of genetic information to the next generation.

MATERIALS AND METHODS

Strains

C. elegans strains were maintained on standard nematode growth media (NGM) plates with *E. coli* OP50 lawns at 20°C. Strains used in experiments include N2 (Bristol) and contained the alleles in the N2 genetic background, as in Table 1.

All experiments performed in the *rnh-1.0 rnh-2* background were performed in F2 (M-/Z-) worms. L4s with wild-type bodies and GFP+ pharynxes (heterozygotes) were picked as the P0s. Subsequently, GFP- F1 L4s were picked to new plates and their progeny (F2) were picked for experimentation unless otherwise noted. CRISPR/Cas9 was used to create the strains indicated in Table 2.

Genome editing was delivered via microinjection of synchronized 1-day-old adult worms performed on 3% agarose pads. Worms were immediately recovered and collected on a single OP50-seeded NGM plate overnight. P0s were singled to individual OP50-seeded plates the next day. Plates with F1 progeny were then screened for *dpy* and/or *rol* phenotypes generated by a *dpy-10* point mutation co-injection marker except in strains with the *mIn1* balancer in which wild-type F1s from each parent were screened. Wild-type F1 siblings were singled to individual plates for screening by PCR and Sanger sequencing in the Carver Center for Genomics (CCG). tracrRNA and crRNAs were obtained from IDT and mixed in the following concentrations for delivery: 14.35 μM Cas9-NLS (Berkeley MacroLab), 17.6 μM tracrRNA (IDT), 1.5 μM *dpy-10* crRNA (IDT), 0.5 μM *dpy-10* ssODN (IDT), 16.2 μM target crRNA (IDT), and 6 μM target ssODN (insertion alleles only, IDT). ssODNs, crRNAs and diagnostic primers can be found in Supplementary Table S1.

Immunofluorescence and image acquisition

10–20 worms were dissected using a #10 razor blade in sperm salts buffer on a 18 × 18 mm coverslip. After gonads extruded, worms were fixed with a 2% PFA solution (1% PFA for S9.6 staining, Figure 2D) and the coverslip was immediately moved to a positively-charged slide. Slides were then transferred to a humidity chamber at room temperature in the dark for 10 min. After fixation, slides were flash-frozen on a dry ice block for 30 min. Coverslips were removed and slides dipped in −20°C methanol for 2 min, followed by a dip in −20°C acetone, and finally washed in 1X PBST (S9.6 1× TBST) for 10 min. For S9.6 slides, a 1:100 dilution of RNase T1 and III in 1× TBST/0.1% BSA/3mM $MgCl_2$ was applied and allowed to incubate on the slides for 1 h at 37°C. Slides were then incubated with 0.5% BSA in 1× PBST for 2 h to block. After BSA treatment, slides were incubated with the primary antibody in a humidity chamber overnight at room temperature in the dark. The next day, slides were washed in 1× PBST for 10 min, incubated with secondary antibody for 2 h in the dark at room temperature, and subsequently washed with 1× PBST for 10 min. Slides were then incubated in the dark

Table 1. Strains used in this publication obtained from *Caenorhabditis* Genetics Center (CGC) or derived from a CGC strain or a combination of CGC strain and strains in Table 2

Strain	Source	Identifier
C. elegans wild-type isolate (Bristol)	CGC	N2
met-2(n4256) III	CGC	MT13293
xpg-1(tm1670) I.	CGC	TG3867
xpf-1(tm2842) II.	CGC	TG1660
mus-81(tm1937) I.	CGC	TG1760
xpg-1(tm1670) I; rnh-2(iow18); rnh-1.0(iow66)/mIn1[mIs14 dpy-10(e128)] II	This study	SSM651
mus-81(tm1937) I; rnh-2(iow18); rnh-1.0(iow66)/mIn1[mIs14 dpy-10(e128)] II	This study	SSM652
spo-11 (ok79) IV / nT1 [qls51] (IV, V)	AV106 (CGC) outcrossed to *nT1 [qls51]*	SSM10
rnh-2(iow18); rnh-1.0(iow66)II/mIn1[mIs14 dpy-10(e128)] II; spo-11 (ok79) IV / nT1 [qls51] (IV, V)	This study	SSM487
top-3::ha::degron(jf122) III; unc-119(ed3) III; ieSi38 [Psun-1TIR-1::mRuby::sun-1 3'UTR, cb-unc-119(+)] IV	CGC	UV207
cku-70(tm1524) III.	CGC	FX1524
rnh-2(iow18); rnh-1.0(iow66)II/mIn1[mIs14 dpy-10(e128)] II; cku-70(tm1524) III	This study	SSM623
cep-1(lg12501) I; unc-119(ed4) III; gtIs1[CEP-1::GFP + unc-119(+)]	CGC	TG12
rpa-2(iow49[3xFLAG::rpa-2])I; rnh-2(iow18); rnh-1.0(iow66)/mIn1[mIs14 dpy-10(e128)] II	This study	SSM655
rpa-2(iow49[3xFLAG::rpa-2])I	(18)	SSM387
syp-3(ok758)/hT2[bli-4(e937) let-?(q782) qIs48] (I;III).	CGC	CV2
ollas::cosa-1; spo-11 (ok79) IV / nT1 [qls51] (IV, V)	(19) and this study	SSM599
rnh-2(iow18); rnh-1.0(iow66)II/mIn1[mIs14 dpy-10(e128)] II; ollas::cosa-1; spo-11 (ok79) IV / nT1 [qls51] (IV, V)	This study	SSM597
rnh-2(iow18); rnh-1.0(iow66)II/mIn1[mIs14 dpy-10(e128)] II; polq-1(tm2026) III	This study	SSM588
rnh-2(iow18); rnh-1.0(iow66)/mIn1 [dpy-10(e128) umnIs43]II; syp-3(ok758)/hT2[bli-4(e937) let-?(q782) qIs48] (I;III	This study	SSM598
met-2(n4256) set-25(n5021) III.	CGC	GW638
polq-1(tm2026) III	CGC	TG2228
set-25(n5021) III.	CGC	MT17463
rnh-2(iow133[degron::rnh-1.0]) II; rnh-1.0(iow17)II; spo-11 (ok79) IV / nT1 [qls51] (IV, V)	This study	SSM594
smIs34 [ced-1p::ced-1::GFP + rol-6(su1006)];	CGC	CU1546
rnh-2(iow18); rnh-1.0(iow66)II/mIn1[mIs14 dpy-10(e128)] II; smIs34 [ced-1p::ced-1::GFP + rol-6(su1006)]	This study	SSM595
syp-3(ok758)/hT2[bli-4(e937) let-?(q782) qIs48] (I;III) smIs34 [ced-1p::ced-1::GFP + rol-6(su1006)]	This study	SSM596

with a 4′,6-diamidino-2-phenylindole (DAPI, 1:10 000 of 5 mg/ml stock in 1× PBST) followed by a final wash in 1× PBST to destain for 10 min. 22 × 22 mm coverslips were then mounted with Vectashield (Vector Laboratories) and sealed with nail polish. Staining for PCN-1 in Figure 5A, PGL-1 in Figure 6C, OLLAS::COSA-1 in Figure 4E, and pH3 in Supplementary Figure S1A was performed as described in [27, 'Antibody staining and image acquisition']. All images were taken using the DeltaVision wide-field fluorescence microscope (GE LifeSciences) with 100×/1.4 NA oil Olympus objective, except in Figures 5A and 6C where a 60× objective was used. Images involving foci counts and DAPI bodies were deconvolved using softWoRx (Applied Precision) at the conservative ratio.

The following antibodies and concentrations were used: Mouse anti-FLAG (Sigma F1803, 1:500), AlexaFluor 488 anti-mouse (Invitrogen A21202, 1:500). Mouse anti-PGL-1 (Made by the Developmental Hybridoma Studies Bank at University of Iowa for the Smolikove Lab, 1:10), AlexaFluor 488 anti-mouse (Invitrogen A21202, 1:500). Mouse anti-DNA–RNA hybrid [S9.6] (Kerafast Kf-Ab01137-2.0, 1:200), AlexaFluor 555 anti-mouse (Invitrogen A28180 1:500). Mouse anti-H3K9me2 (Abcam 1220, 1:200), AlexaFluor 488 anti-mouse (Invitrogen A28180, 1:500). Rabbit α-RAD-51 (Custom made by Genscript for the Smolikove lab, 1:30,000), Alexa Fluor 488 α-mouse (Invitrogen A21202, 1:500) (Invitrogen A31570, 1:500). Rabbit α-PCN-1 (Gift from M. Michael, 1:13000 (20)), Alexa Fluor 488 α-rabbit (Molecular Probes/Invitrogen, A32790, 1:500). Rabbit α-pH3 (Upstate Biotechnologies 06–570, 1:5000), Alexa Fluor 488 α-rabbit (Molecular Probes/Invitrogen, A32790, 1:500). Rabbit Phospho-ATM/ATR Substrate Motif [(pS/pT) QG] (Cell Signaling 6966S, 1:100), rabbitanti-OLLAS 1:1000 (A01658, Genscript). Rabbit anti-pCDK-1 (Cell Signaling 9111T, 1:500), AlexaFluor 488 α-rabbit (Molecular Probes/Invitrogen, A32790, 1:500). Rabbit anti-CHK-1 (Cell Signaling 4539, 1:100), AlexaFluor 488 α-rabbit (Molecular Probes/Invitrogen, A32790, 1:500), and mouse anti-fibrillarin (72B9, gift from P. DiMario).

Whole body fixation and DAPI staining

For DAPI body experiments and CED-1::GFP analysis, 10 worms per slide were picked into a droplet of M9 buffer on an uncharged slide (Surgipath Leica). M9 was removed using Whatman filter paper and 8ul of absolute ethanol was added to the worms and allowed to evaporate. For preservation and chromatin staining, 8 ul DAPI/Vectashield (Vector Laboratories) was added to the slide and a 22 × 22 mm coverslip was affixed and sealed with nail polish.

DNA–RNA hybrids dot blot

Plates of the selected genotypes were washed with 30% sucrose, spun down, and washed three times with M9 buffer until little to no bacteria was visible in the tube. Lysis buffer containing 100 mM Tris pH 8.5, 50 mM EDTA, 200 mM NaCl, 0.5% sodium dodecyl sulfate (SDS), and 0.05% 20 mg/ml Proteinase K was then added to the pelleted worms and flash frozen in liquid nitrogen. Worm-containing solution was then incubated at 65°C for 1 h with consistent spinning until cleared. Large-scale genomic DNA was extracted via phenolchloroform/isoamyl extraction and eluted in Qiagen elution buffer (Tris). To control for RNA targets of the S9.6 monoclonal antibody, RNase T1 and III in 30 mM $MgCl_2$, 200 mM Tris, 500 mM NaCl, pH 7.5 RNaseT1/III buffer was added to the tubes. In RNaseH-treated controls, 1× NEB RNaseH buffer and RNaseH were added and an equal volume of additional RNase T1/III buffer was added to non-control tubes. All tubes were then incubated at 37°C for 30 min. 2 μg of each DNA was then applied to a prewetted nylon membrane in a Bio-Rad dot blot apparatus and connected to a vacuum manifold until wells were dry. DNA was UV crosslinked to the membrane and blocked with 5% milk in 1× PBST with agitation for 1 h. The membrane was then incubated with a 1:500 dilution of the S9.6 primary antibody (Kerafast Kf-Ab01137-2.0) in 1× PBST in the dark overnight at 4ºC with agitation. The next morning the membrane was washed twice with 1× PBST for 10 min and incubated in goat α-Mouse IgG (Kappa light chain) HRP 1:1000 with agitation for 2 h. The membrane was then washed three times with 1× PBST for 10 min each and using WesternBright ECL (#K-12045-D20; Advansta), blots were exposed using the LI-COR Odyssey Infrared Imaging System.

DNA–RNA immunoprecipitation (DRIP) RT-qPCR

DNA extraction and control for RNA/RNaseH were added as in dot blot (see above). Following incubation for 30 min at 37ºC, AseI enzyme (New England Biosciences, R0526L) was added and allowed to incubate at 37ºC for an additional 4 h. BstUI enzyme (New England Biosciences, R0518L) was then added and incubated at 60ºC for 4 h. DNA was then incubated with 2 μl/μg S9.6 primary antibody (Kerafast Kf-Ab01137-2.0) and 2× binding buffer containing 10 mM $NaPO_4$, 140 mM NaCl and 0.5% Triton over night at 4ºC in the dark with agitation. The next day, the antibody-bound DNA was immunoprecipitated with magnetic Dynabeads® IgGA, suspended in 1X TE and DNA–RNA hybrids released by digesting the antibody with Proteinase K (New England Biosciences, P8107S 20 mg/ml) at 60ºC for 1 h. Following purification (ZymoResearch Clean & Concentrator-5, D4013), cDNA was synthesized using the iScript cDNA synthesis kit (Bio-Rad Laboratories, 1708890) and distributed to wells with 5μM primers for the indicated loci (primers available in Supplementary Table S2) and 2X iQ SYBR Green supermix (Bio-Rad #1708880). RT-qPCR was performed in white 96-multiwell plates (Roche, 04729692001) with adhesive film on an Applied Biosciences QuantStudio 3 in the Carver Center for Genomics (CCG). To ensure robust and accurate quality, 3 technical replicates of each immunoprecipitation product (wild type, *met-2*, *rnh-1.0 rnh-2* M-/Z-) were run per locus per RT-qPCR experiment. 3 biological replicates of each population were performed to this standard. Primers used are listed in Supplementary Table 2.

Table 2. Strains created via CRISPR/Cas9 for this publication

Strain	Identifier
rnh-1.0(iow118[FLAG::rnh-1.0isoc])II	SSM545
rnh-2(iow124[3XFLAG::rnh-2]) II	SSM582
rnh-2(iow18); rnh-1.0(iow66)II/mIn1[mIs14 dpy-10(e128)] II.	SSM422
rnh-2(iow133[degron::rnh-1.0]) II; rnh-1.0(iow17)II	SSM608
rnh-2(iow18); rnh-1.0(iow134)/mIn1 [dpy-10(e128) umnIs43]II	SSM614
rnh-2(iow18) rnh-1.0(iow66) xpf-1(tm2842)/mIn1[mIs14 dpy-10(e128)] II	SSM578

Focus quantification

Foci were quantified in SoftWoRx software using deconvolved images in all experiments. Protocols for focus quantification were based on RAD-51 focus quantification protocols (21,22). Background foci were eliminated by reducing channel intensity until staining was only visible within nuclei (threshold of no more than five cytoplasmic foci), except in S9.6 staining (Figure 2D) where DNA–RNA hybrids could form in the cytoplasm and therefore the 'restore defaults' option in SoftWoRx software was used only. Often this reduced the number of foci reported to a value below what we would expect from looking at uncorrected images. Only foci colocalized with chromatin staining are reported.

Checkpoint assay and nuclear diameter

Checkpoint activation in Figure 5D–F was performed as described in (23). Nuclear diameters were measured in SoftWoRx software using the 'measure' tool. Reported diameters are the average of the X and Y measurements of the nuclei as determined by the bounds of chromatin staining.

Fluorescence intensity measurements

All fluorescence intensity measurements were taken in non-deconvolved images in Fiji ImageJ software. Within each gonad, measurements were taken of nuclei in the same Z-plane and corrected against the average background (cytoplasmic) of the gonad in the same plane.

Auxin Treatment

Worms of the indicated genotype were picked as L4s on OP50-seeded NGM plates containing 1 mM 3-Indoleacetic acid (i.e. auxin, Alfa Aesar A10556-22) dissolved in absolute ethanol and maintained at 20°C for the specified times.

Acridine orange

Acridine orange staining was performed on synchronized 1-day-old adult worms. Worms were transferred to a tube of 10mg/ml acridine orange diluted 1:400 in M9, immediately covered with aluminum foil, and allowed to rotate on

a mixer for 2 h. After incubation, worms were transferred to a clean NGM plate. Worms were then placed onto freshly prepared 10% agarose pads with 8 ul M9 and 2 ul of Polybead 0.1-um polystyrene beads (#00876; Polysciences), before imaging on the DeltaVision wide-field fluorescent microscope at 60× magnification. Levels of acridine orange-stained nuclei were scored where nuclei that stained positive were counted towards the total.

EdU pulse chase

Synchronized 1-day-old adults of the indicated genotypes were picked into 50 μl M9 buffer and 1 mM EdU (Click-iT EdU kit, ThermoFisher 555) was added to the tube and incubated in the dark at 20ºC for the indicated amount of time. Worms were then recovered to an OP50-seeded NGM plate for 20 min and dissected in 1× PBS. Dissected gonads were fixed in a 3.7% PFA solution and incubated in a humidity chamber at 20ºC in the dark for 10 min. Slides were freeze-cracked on a dry ice block for 30 min, the coverslips removed, and dipped in –20ºC methanol for 20 min. Slides were then washed with 1× PBST three times for 10 min each. EdU processing solution was applied as directed by the manufacturer for 1 h in the dark at 20ºC and subsequently washed three times in 1× PBST for 10 min each. Chromatin staining was performed by dipping the slides in 1:10 000 dilution DAPI (5 mg/ml) in 1× PBST for 20 min and destaining in 1X PBST twice for 5 min each. 22 × 22 mm coverslips were affixed with Vectashield and sealed with nail polish.

Statistical methods

All statistics reported in this manuscript were calculated using GraphPad Prism 9 software. Where multiple groups were compared and non-parametric data used, Kruskal-Wallis tests were applied with multiple comparisons using the two-stage linear set-up procedure of Benjamini, Krieger and Yekutieli to control for false positives. When q-values were significant ($q < 0.05$), statistical significance was reported from Mann–Whitney analysis. When multiple groups were compared and parametric data used, a one-way ANOVA with multiple comparisons was applied using the two-stage linear set-up procedure of Benjamini, Krieger and Yekutieli to correct for false discovery. When q-values were significant ($q < 0.05$), an unpaired t-test was applied. For comparisons between untreated and RNaseH-treated controls in DRIP RT-qPCR, a paired t-test was applied. In Figures 1D, 3C, D, 5A, C, Supplementary Figures S1A, S5A where quantification was of yes/no values, a Fisher's exact t-test was applied between groups on a 2 × 2 contingency table.

Sample sizes

Figure 1, panel C n-values for nuclei of FLAG::RNH-1.0 fluorescence intensity were, respectively: 29, 38, 35, 32 (PMT, TZ, MP, LP). Values for nuclei of FLAG::RNH-2 fluorescence intensity were, respectively: 28, 31, 48, 40 (PMT, TZ, MP, LP). Panel D, n-values for FLAG localization based on nuclear cell cycle stage were, for FLAG::RNH-1.0 89/98 (interphase), 6/98 (metaphase) and 3/98 (telophase) and for FLAG::RNH-2 131/138 (interphase), 4/138 (metaphase), 3/138 (telophase). At least three gonads were analyzed for all panels in Figure 1.

Figure 2, panel A and B, 10 N2, 10 *rnh-1.0 rnh-2* M+/Z-, and 7 *rnh-1.0 rnh-2* M-/Z- parents were scored from. The number of dots quantified in panel C were 6, 6, and 5 per blot. Dot blot was performed with at least five technical replicates and the experiment was repeated 3 times with new extracts, constituting 3 biological replicates. In panel G, the number of nuclei in which foci were counted were, in wild type, 393 (PMT), 350 (TZ), 323 (MP), 217 (LP) and in *rnh-1.0 rnh-2 M-/Z-* 241 (PMT), 354 (TZ), 280 (MP), 203 (LP). At least six gonads were counted for both genotypes. For DRIP RT-qPCR in panel H, 3 technical repeats were performed per run and RT-qPCR was run 3 times with new extracts each time, constituting three biological repeats.

Figure 3, panel A, the number of nuclei in which RAD-51 foci were counted for wild-type were, from zone 1 to zone 7 respectively: 200, 156, 136, 174, 166, 118, 100. From zone 1 to zone 7, the number of nuclei counted in *rnh-1.0 rnh-2 M+/Z-* germlines was: 98, 119, 107, 80, 74, 60, 63. *rnh-1.0 rnh-2 M-/Z- n*-values were, from zone 1 to zone 7: 66, 85, 69, 85, 72, 62, 28. At least three gonads of each background were analyzed. In panel E, the number of nuclei analyzed were, in wild-type from zone 1 to zone 7, respectively: 109, 110, 150, 140, 116, 87, 50, in *rnh-1.0 rnh-2 M-/Z-* 66, 85, 69, 85, 72, 62, 28, and in *rnh-1.0 rnh-2::AID* 54, 59, 57, 74, 51, 63, 31. At least three gonads were analyzed in all backgrounds. In panel F, 21 wild-type oocytes were counted, 21 *rnh-1.0 rnh-2 M+/Z-* oocytes, and 36 *rnh-1.0 rnh-2 M-/Z-* oocytes. In panel H, 31 wild-type oocytes, 33 *rnh-1.0 rnh-2 M+/Z-,* and *30 rnh-1.0 rnh-2::AID* oocytes were counted. In panel G, 33 wild type, 27 *xpg-1*, 31 *mus-81,* 25 *xpf-1*, 62 *rnh-1.0 rnh-2 M-/Z-,* 29 *rnh-1.0 rnh-2; xpg-1 M-/Z-,* 34 *mus-81;rnh-1.0 rnh-2,* and 23 *rnh-1.0 rnh-2 xpf-1* oocytes were counted. For DAPI body counts in panel I, 73 wild-type, 38 *cku*-70, 35 *polq-1,* 65 *rnh-1.0 rnh-2* M-/Z-, 38 *rnh-1.0 rnh-2;cku-70* M-/Z- and 37 *rnh-1.0 rnh-2; polq-1* M-/Z- oocytes were analyzed

Figure 4, panel A, the number of nuclei analyzed was, from zone 1 to zone 7 respectively: 122, 122, 122, 102, 117, 90, 73 (wild type), 95, 145, 136, 93, 87, 58, 54 (*spo-11; rnh-1.0 rnh-2 M+/Z-*) and 75, 93, 100, 71, 76, 70, 62 (*rnh-1.0 rnh-2;spo-11 M-/Z-*). At least three gonads were analyzed in each background. In panel C, 21 wild-type, 36 *rnh-1.0 rnh-2 M-/Z-,* 36 *spo-11;rnh-1.0 rnh-2 M-/Z-,* and 36 *spo-11* oocytes were counted. In panel E, 41 wild type, 46 *spo-11,* and 50 *rnh-1.0 rnh-2;spo-11* late pachytene nuclei were scored. In panel F, 46 wild-type, 31 *rnh-1.0 rnh-2::AID*, 42 wild-type + auxin, 30 *rnh-1.0 rnh-2::AID* + auxin, and 39 *rnh-1.0 rnh-2::AID* + auxin/60h NGM oocytes were counted. In panel G, 33 wild-type, 27 *xpg-1,* 31 *mus-81,* 25 *xpf-1,* 62 *rnh-1.0 rnh-2* M-/Z-, 29 *rnh-1.0 rnh-2;xpg-1* M-/Z-, 34 *mus-81;rnh-1.0 rnh-2* M-/Z- and 23 *rnh-1.0 rnh-2 xpf-1* M-/Z- diakinesis –1 DAPI bodies were counted.

Figure 5, panel A, the number of PCN-1-positive and -negative nuclei were scored in 4 gonads of each genotype. In panel C, the number of FLAG::RPA-2 'haze-' positive and negative nuclei were scored in 3 gonads of each genotype. In

panel E, 60 wild-type, 44 wild-type + HU, 68 *rnh-1.0 rnh-2 M-/Z-* and 42 *rnh-1.0 rnh-2 M-/Z-* + HU PMT nuclear diameters were measured. In panel F, 94 wild-type, 73 wild-type + HU, 100 *rnh-1.0 rnh-2 M-/Z-* and 68 *rnh-1.0 rnh-2 M-/Z-* PMT nuclear diameters were measured. For RAD-51 foci counts in panel G, 79 wild-type, 54 wild-type + HU, 54 *rnh-1.0 rnh-2 M-/Z-* and 55 *rnh-1.0 rnh-2 M-/Z-* nuclei were analyzed. For pS/pT) QG foci counts in zones 1 and 2 in panel I, 85 zone 1 and 92 zone 2 nuclei were (analyzed in wild type and in *rnh-1.0 rnh-2 M-/Z-* 35 zone 1 and 32 zone 2 nuclei were counted. For fluorescence intensity measurements of CDK-1 in panel J, 206 wild-type, 96 *rnh-1.0 rnh-2 M-/Z-* and 125 *top-3::ha::AID* nuclei were measured. In all panels, at least three gonads were analyzed.

Figure 6, panel A, CED-1::GFP engulfment was scored in 51 wild-type, 26 *rnh-1.0 rnh-2 M+/Z-*, 22 *syp-3*, and 27 *rnh-1.0 rnh-2 M-/Z-* pachytene nuclei. Acridine orange staining in panel B was scored in 43 wild-type, 46 *rnh-1.0 rnh-2 M-/Z-,* 41 *rnh-1.0 rnh-2;cku-70 M-/Z-*, 45 *rnh-1.0 rnh-2;polq-1*, 35 *met-2*, 36 *set-25,* 32 *met-2;set-25* and 45 *syp-3* germlines. Scoring for PGL-1 in panel C was done in 283 wild-type and 271 *rnh-1.0 rnh-2* M-/Z- late pachytene nuclei. In panel D, from zones 1 to 7 respectively, the number of nuclei in which FLAG::RPA-2 foci were counted was: 22, 31, 55, 47, 41, 36, 31 (wild type), 35, 60, 52, 65, 46, 35, 22 (*rnh-1.0 rnh-2 M-/Z-*). For fluorescence intensity measurements of (pS/pT) QG localization, the number of nuclei from zone 1 to zone 7 was: 34, 46, 39, 60, 58, 40, 31 (wild type), 25, 32, 38, 52, 38, 34, 45 (*syp-3*) and 41, 80, 92, 63, 61, 35, 30 (*rnh-1.0 rnh-2 M-/Z-*) and 26, 58, 63, 66, 59, 36, 33 (*rnh-1.0 rnh-2;syp-3)*. For the number of CHK-1 foci counted in late pachytene nuclei in panel G, 88 wild-type and 69 *rnh-1.0 rnh-2 M-/Z-* LP nuclei were analyzed. For CEP-1::GFP fluorescence intensity measurements in panel H, 28 wild-type, 25 *rnh-1.0 rnh-2* M-/Z-, and 30 *rad-51(RNAi)* LP nuclei were measured. All experiments in this figure were performed in at least 3 gonads.

RESULTS

RNaseH1 and RNase H2 localize to germline nuclei

The *C. elegans* genome encodes for four RNaseH1 proteins and one RNaseH2 protein (24). Of the four isoforms of *rnh-1* in *C. elegans,* only *rnh-1.0* possesses both canonical domains of RNaseH1 (25), making it the most likely candidate for RNaseH1 function (Figure 1A). To assess if RNaseH is germline-expressed, we generated FLAG::RNH-1.0 and FLAG::RNH-2 using CRISPR/Cas9 at the endogenous locus. Immunohistochemistry (IHC) for FLAG and measurement of the fluorescence intensity in germline nuclei identified that both RNH-1.0 and RNH-2 are widely expressed in germline nuclei (Figure 1B and Supplementary Figure S1A). Importantly, RNaseH1 and RNaseH2 were enriched in the pre-meiotic tip nuclei (PMT) of the germline, reflecting their known function in replication, as well as in all stages of meiotic prophase I, suggesting a potential and previously undescribed role for RNaseH in meiosis (Figure 1C). We next chose to identify RNH-1.0 and RNH-2 localization throughout the cell cycle (Figure 1D). Cell cycle stage was determined by chromatin morphology visualized by DAPI staining combined with phospho-histone H3 (pH3) staining (26). Nuclei exhibiting compact DAPI staining were defined as M-phase nuclei, most of which were also positive for pH3 [Supplementary Figure S1B]. The large majority of interphase nuclei contained both FLAG::RNH-1.0 and FLAG::RNH-2. M-phase nuclei were mostly negative for FLAG::RNH-1.0, but FLAG::RNH-2 was present in about half of M-phase cells, mostly after anaphase onset (transition from one to two proximal compact DAPI staining bodies). These observations taken together suggest that RNaseH acts in the PMT within S/G2 phase nuclei, consistent with studies in other organisms (27).

RNaseH1/2 is required for maintaining low levels of R-loops, possibly on highly-transcribed germline genes

To determine the role of R-loops in meiosis we generated null mutants in the *rnh-1.0* and *rnh-2* genes using CRISPR/Cas9. While single mutants exhibited no observable phenotypes, double mutants showed impaired gametogenesis, as elaborated below. *rnh-1.0 rnh-2* worms that are the progeny of heterozygous mothers (M^+/Z^-) have a comparable brood size and viability to wild type. However, their *rnh-1.0 rnh-2* progeny (M^-/Z^-) show both severe reduction in brood size and loss of embryonic viability (Figure 2A-C). We attribute this significant effect to increased nuclear divisions from the first and second generations and maternal contribution of wild-type *rnh-1.0* and *rnh-2* in M^+Z^- worms. Given that M^-/Z^- worms do exhibit all stages of meiosis, we performed all experiments on *rnh-1.0 rnh-2* M^-/Z^- worms unless otherwise noted.

It is expected that *rnh-1.0 rnh-2* mutants experience an accumulation of R-loops. We performed a dot blot of genomic DNA using the monoclonal S9.6 antibody specific to DNA–RNA hybrids (Figure 2D). Relative to the wild-type control, *rnh-1.0 rnh-2* mutants display a robust enrichment for DNA–RNA hybrids on the genomic level. To compare the level of the R-loop signal we performed side-by-side analysis of a previously studied mutant, *met-2*. MET-2 acts in the pathway that downregulates R-loops specifically at DNA transposons and repeat elements and *met-2* mutants are phenotypically indistinguishable from *met-2; set-25* double mutants for their function in R-loop repression (14,15). *rnh-1.0 rnh-2* mutants exhibit a dramatic increase in DNA–RNA hybrids compared to *met-2* (Figure 2D). To assess whether this effect extended specifically to germline nuclei, we stained for DNA–RNA hybrids in dissected gonads. We detected an increase of DNA–RNA hybrids in the mitotic region of the germline (PMT), as well as early meiotic prophase [transition zone (TZ) and mid-pachytene (MP)] regions of *rnh-1.0 rnh-2* gonads compared to wild type (Figure 2E and F), regions that express the RNAseH proteins (Figure 1B and C).

Unlike *met-2* mutants, *rnh-1.0 rnh-2* mutants do not have a decrease in H3K9 methylation (Supplementary Figure S1C), suggesting that RNAseH has different targets than MET-2. A transcriptomic analysis of the *C. elegans* germline identified the most highly-expressed germline genes (28). Because R-loop formation is canonically associated with transcription, we reasoned that the accumulation of DNA–RNA hybrids in *rnh-1.0 rnh-2* germlines should occur at these loci. In order to test this hypothesis,

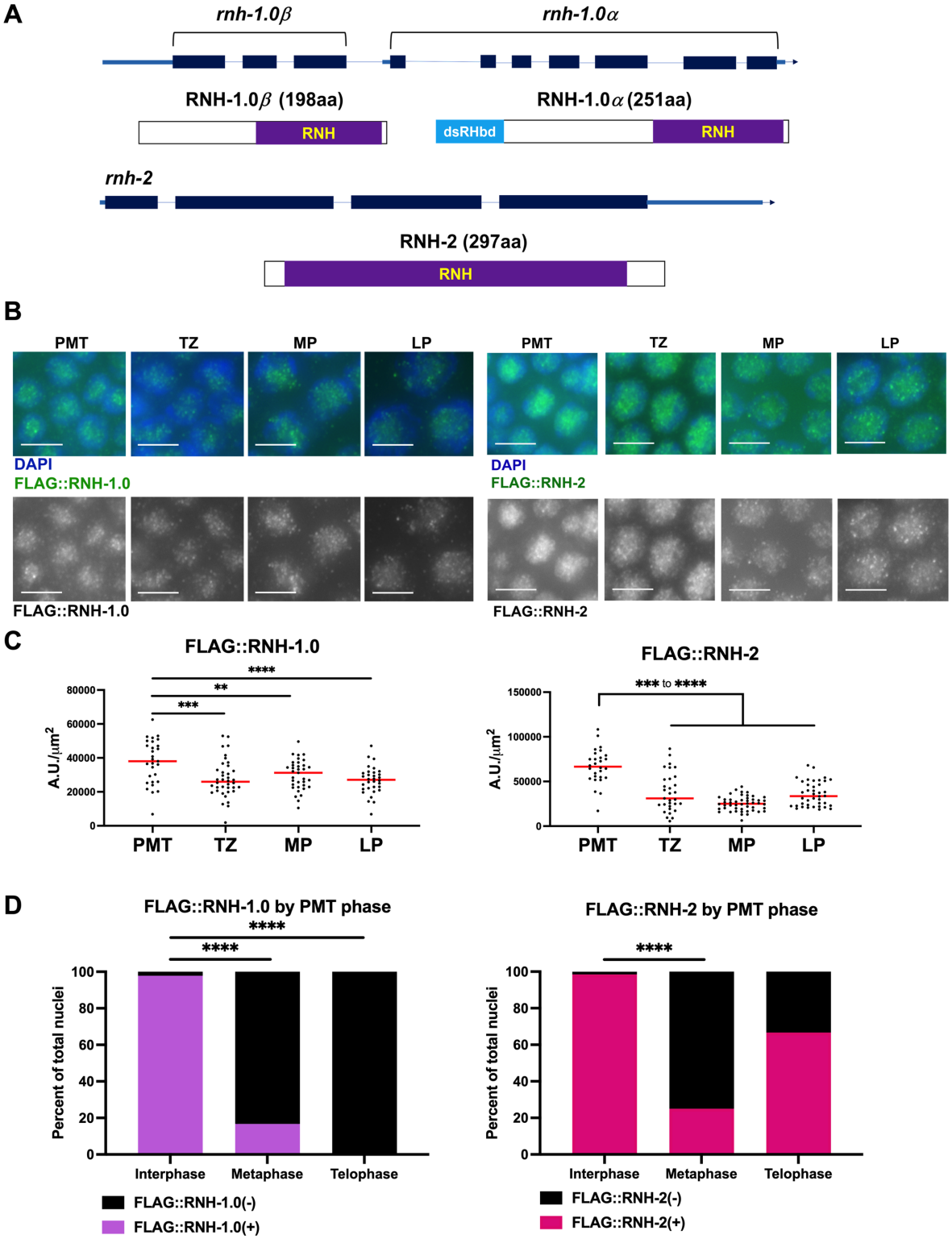

Figure 1. RNaseH enzymes localize to germline nuclei. (**A**) Representative diagram of the two isoforms of RNH-1.0 (40) and RNH-2 (bottom) and their functional domains in *C. elegans.* Dark blue boxes represent exons. 'RNH' in purple boxes represent the annotated RNaseH domains and 'dsRHbd' in light blue represents the double-stranded RNaseH binding domain of RNH-1.0 (**B**) Representative images of FLAG::RNH-1.0 (left) and FLAG::RNH-2 (right) localization in indicated germline regions (PMT = pre-meiotic tip, TZ = transition zone, MP = mid-pachytene, LP = late pachytene). Scale bar 4 μm. (**C**) Quantification of FLAG::RNH-1.0 (left) and FLAG::RNH-2 (right) fluorescence intensity corrected against cytoplasmic background signal. X-axis indicates region of the germline (as in (B)) and y-axis indicates arbitrary fluorescence intensity units per μm^2. Each data point represents the fluorescence intensity of one nucleus. Asterisks indicate statistical significance calculated by Mann–Whitney *t*-test (****$P < 0.0001$, ***$P < 0.001$, **$P < 0.01$ and *$P < 0.05$). Red lines indicate median. (**D**) Localization of FLAG::RNH-1.0 (left) and FLAG::RNH-2 (right) to nuclei in the pre-meiotic stem cell niche by nuclei cell cycle phase as determined by chromatin morphology.

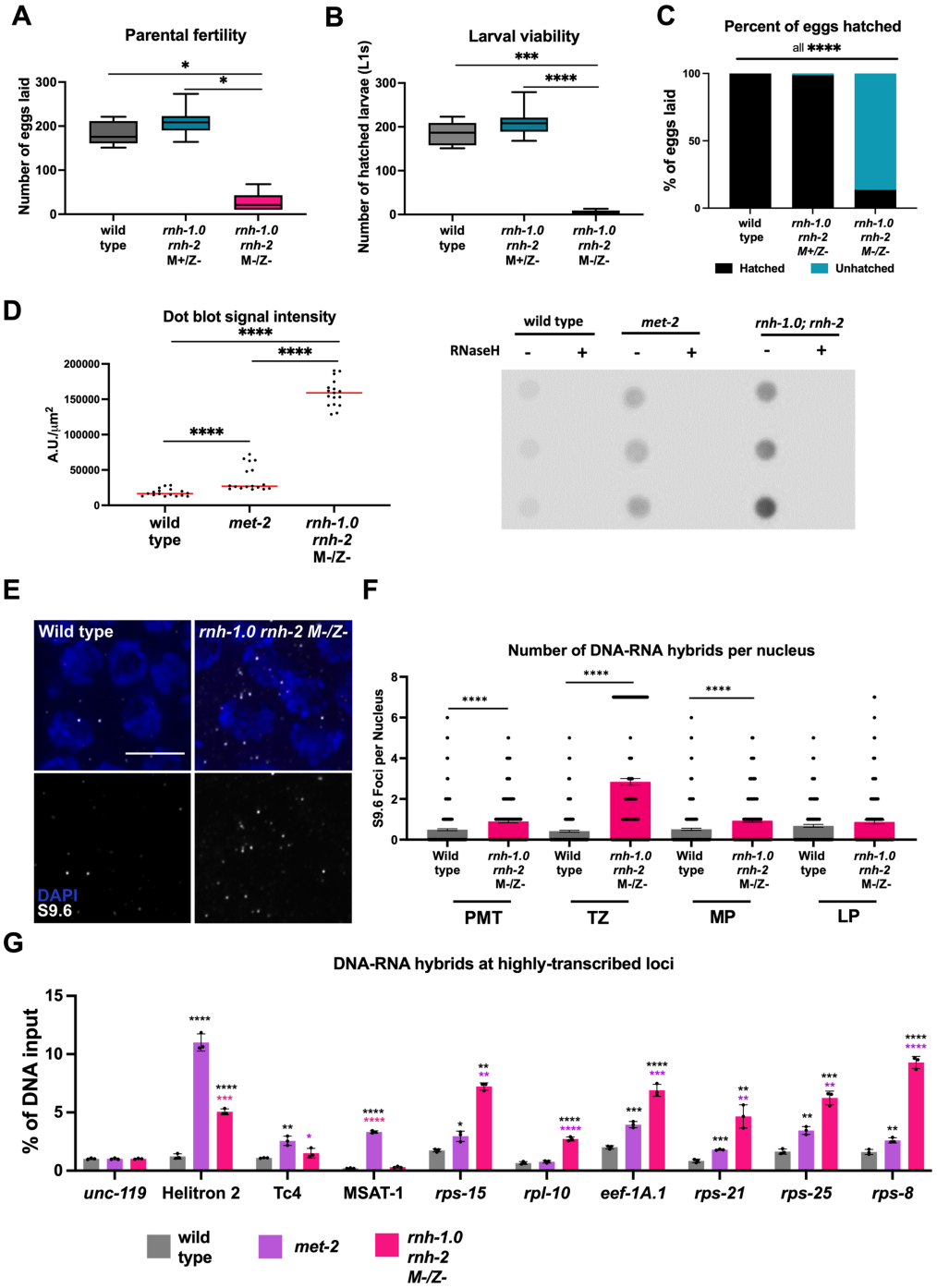

Figure 2. The absence of RNaseH enzymes accumulates R-loops in the germline at highly-transcribed regions. (**A**) Quantification of the number of eggs laid by parents in the indicated backgrounds and generations. Asterisks indicate statistical significance calculated by Mann–Whitney *t*-test (****$P < 0.0001$, ***$P < 0.001$, **$P < 0.01$ and *$P < 0.05$). (**B**) Quantification of viable L1 larvae from parents of the indicated backgrounds and generations. Asterisks indicate statistical significance calculated by Mann–Whitney *t*-test (****$P < 0.0001$, ***$P < 0.001$, **$P < 0.01$ and *$P < 0.05$). (**C**) Percent of eggs hatched Asterisks indicate statistical significance calculated by Fisher's exact test (**D**) *Top*-representative dot blot for DNA–RNA hybrids in the genotypes indicated at top with (+) or without (–) provision of RNaseH. *Bottom*: Quantification of dot blot signal intensity calculated with background signal correction. Each data point represents the signal intensity of one dot. Red lines denote the median. Asterisks indicate statistical significance calculated by Mann–Whitney *t*-test (****$P < 0.0001$, ***$P < 0.001$, **$P < 0.01$ and *$P < 0.05$). (**E**) Representative image of DNA–RNA hybrids in TZ. For immunofluorescence specifically, RNaseT1 and RNaseIII were used prior to application of S9.6 antibody. Scale bar 4 μm. (**F**) Quantification of the number of S9.6 foci (i.e. DNA–RNA hybrids) in regions of the germline. Each data point represents the number of foci in one nucleus. Error bars reflect mean with SEM. Asterisks indicate statistical significance calculated by Mann–Whitney t-test (****$P < 0.0001$, ***$P < 0.001$, **$P < 0.01$ and *$P < 0.05$). (**G**) DRIP RT-qPCR results for the control locus (*unc-119*), three unexpressed loci, and the six most highly-expressed germline loci (7) as a function of the percentage of total input DNA. Each data point represents the average value of three technical repeats in one run of RT-qPCR. Error bars represent mean with SEM. Black asterisks indicate statistical significance to wild type, pink asterisks to *rnh-1.0 rnh-2*, and purple asterisks to *met-2*. Statistical significance calculated by unpaired t-test (****$P < 0.0001$, ***$P < 0.001$, **$P < 0.01$ and *$P < 0.05$).

DNA–RNA hybrids were immunoprecipitated from whole worm extracts, reverse transcribed and a quantitative PCR (DRIP RT-qPCR) was performed with primers for some of the most highly-expressed germline loci and loci identified as prone to DNA–RNA-hybrid accumulation in *met-2;set-25* mutants (14). While DNA–RNA hybrids did not accumulate in *rnh-1.0 rnh-2* mutants more than in wild type or *met-2* worms at *unc-119*, Tc4 or MSAT-1 loci (low/no germline expression), a significant enrichment was detected at the highly-transcribed loci *rps-8*, *rps-15, rps-21, rps-25, rpl-10* and *eef-1A.1* (Figure 2G). As expected from our analysis of H3K9 methylation, *met-2* and *rnh-1.0 rnh-2* mutants had different effects on the genes tested: while *rnh-1.0 rnh-2* mutants showed higher levels of DNA–RNA hybrid accumulation on highly transcribed genes, DNA–RNA hybrids accumulated on repetitive loci in *met-2* mutants. Basal levels of DNA–RNA hybrids were identified in samples pretreated with RNAseH (Supplementary Figure S1D) Interestingly, in wild-type nuclei, the bulk of the RNH-1.0 and RNH-2 signal colocalize with fibrillarin, a marker of the nucleolus and a highly-transcribed nuclear compartment (Supplementary Figure S1E). Taken together, these results indicate that R-loops accumulate in *C. elegans* germline nuclei and suggest that they may do so at natural, highly-transcribed meiotic loci.

RNaseH1/2 is required for preventing irreparable breaks

The prevailing model states that an overaccumulation of R-loops generates DSBs as a result of replication–transcription conflicts (1,2). Therefore, we sought to assess DSB formation in the *rnh-1.0 rnh-2* background. DSBs in meiosis are preferentially channeled for repair by HR which capitalizes on the availability of a homologous template to ensure error-free repair (8,9). Processing of the break site results in 3′ single-stranded DNA (ssDNA) on which the recombinase RAD-51 is loaded to direct the homology search and promote strand invasion of the homolog. Therefore, we used RAD-51 as a marker for processed DSBs in *rnh-1.0 rnh-2* germlines and quantified the average number of RAD-51 foci per nucleus to reflect DNA damage levels (Figure 3A and B). The germline up to (and including) late pachytene was divided into seven 33 nm-long non-overlapping sections, arranged from the distal (mitotic nuclei of the stem cell niche) to the proximal germline (meiotic pachytene nuclei). Each one of these sections is defined as a 'zone' and the number of RAD-51 foci per nucleus in each one of these zones was plotted. The results of this analysis indicate a marked increase in DSB formation as a result of R-loop accumulation across the entire germline (Figure 3A and B). We also tested this effect at 25^{o}C, as *met-2* mutants showed a loss of viability after shifting to a higher temperature, an effect which was attributed to elevated DNA damage levels (14,15), however there was no increase in RAD-51 focus formation in *rnh-1.0 rnh-2* mutants at the higher temperature (Supplementary Figure S2A). Intriguingly, damage foci persisted beyond late pachytene, where crossovers have already formed and synaptonemal complex (SC) disassembly begins and were observed in diplotene and diakinesis (Figure 3C and D). The prevalence of these damage foci beyond pachytene suggests that a significant fraction of DSBs remain unrepaired throughout meiosis and pose a threat to the genomic integrity of the gametes. To confirm that these phenotypic effects are of germline-origin, we exploited the auxin-inducible degradation system to generate an auxin-inducible *rnh-2* allele (*rnh-2::AID*) in the *rnh-1.0* background under the germline-specific *sun-1* promoter (29). With this design, any effects seen would be due only to loss of *rnh-2* in the germline of *rnh-1.0* null mutants. In agreement, RAD-51 foci accumulated in germline nuclei of *rnh-1.0 rnh-2::AID* in similar numbers to that of the null mutants (Figure 3B and E).

To determine whether the persistent DSBs seen in diplotene and diakinesis confer chromosomal aberrations in the oocytes, we quantified the number of DAPI-stained bodies in the final oocyte of *rnh-1.0 rnh-2* germlines. A wild-type *C. elegans* genome is composed of six homologous chromosome pairs (bivalents) connected by chiasmata (*i.e.* six DAPI bodies)(9). Deviations from this number can be reflective of fusion events, univalents, or chromosome fragments. While fusion events manifest as DAPI body counts of less than six, univalents and chromosome fragments are scored as more than six DAPI bodies. In *rnh-1.0 rnh-2* $M^{-}Z^{-}$ diakinesis, only ∼20% of oocytes contained a wild-type number of DAPI bodies, while the remaining ∼80% had up to 11 DAPI bodies as a result of chromosome fragmentation (Figure 3F and G). Aside from fragments, intact chromosomes maintained the characteristic appearance of a bivalent. This phenotype was only observed in the *rnh-1.0 rnh-2* double mutant; *rnh-1.0* and *rnh-2* single mutants had wild-type numbers of DAPI bodies even after passaging for 20 generations, reflecting the functional redundancy of *rnh-1.0* and *rnh-2* (Supplementary Figure S2B). We also quantified the number of DAPI bodies in *rnh-1.0 rnh-2::AID* M-/Z- diakinesis oocytes and observed chromosome fragmentation much like in *rnh-1.0 rnh-2* knockout worms (Figure 3G and H). When DSB repair is perturbed in the *C. elegans* germline (*i.e.* mutants in HR pathway), DSBs can be repaired via classical non-homologous end joining (cNHEJ) or theta-mediated end Joining (TMEJ) [also called microhomology-mediated end joining (MMEJ)](9). Repair by these pathways leads to chromosomal fusions and abrogating this pathway thus leads to an increase in DAPI body numbers (10,11,30). To test if cNHEJ or TMEJ contribute to DSB repair we analyzed DAPI body numbers in the triple mutants *rnh-1.0 rnh-2; cku-70* and *rnh-1.0 rnh-2; polq-1,* that abrogate cNHEJ and TMEJ respectively (Figure 3I). In both mutants we observed no change in DAPI body number indicating that these pathways are not involved in DSB repair in *rnh-1.0; rnh-2* mutants. These findings are consistent with the fact that we did not observe a significant decrease (below 6) in DAPI body numbers, as observed when these pathways are activated in recombination-deficient mutants. Altogether these data suggest that excessive R-loop-generated DSBs (∼15 DSBs/nucleus) are either repaired by HR (generating bivalents) or not at all (generating chromosomal fragments) and not targeted to alternative repair pathways. The latter is indicative of a germline-specific, unique type of DSB conferred by R-loops which cannot be repaired.

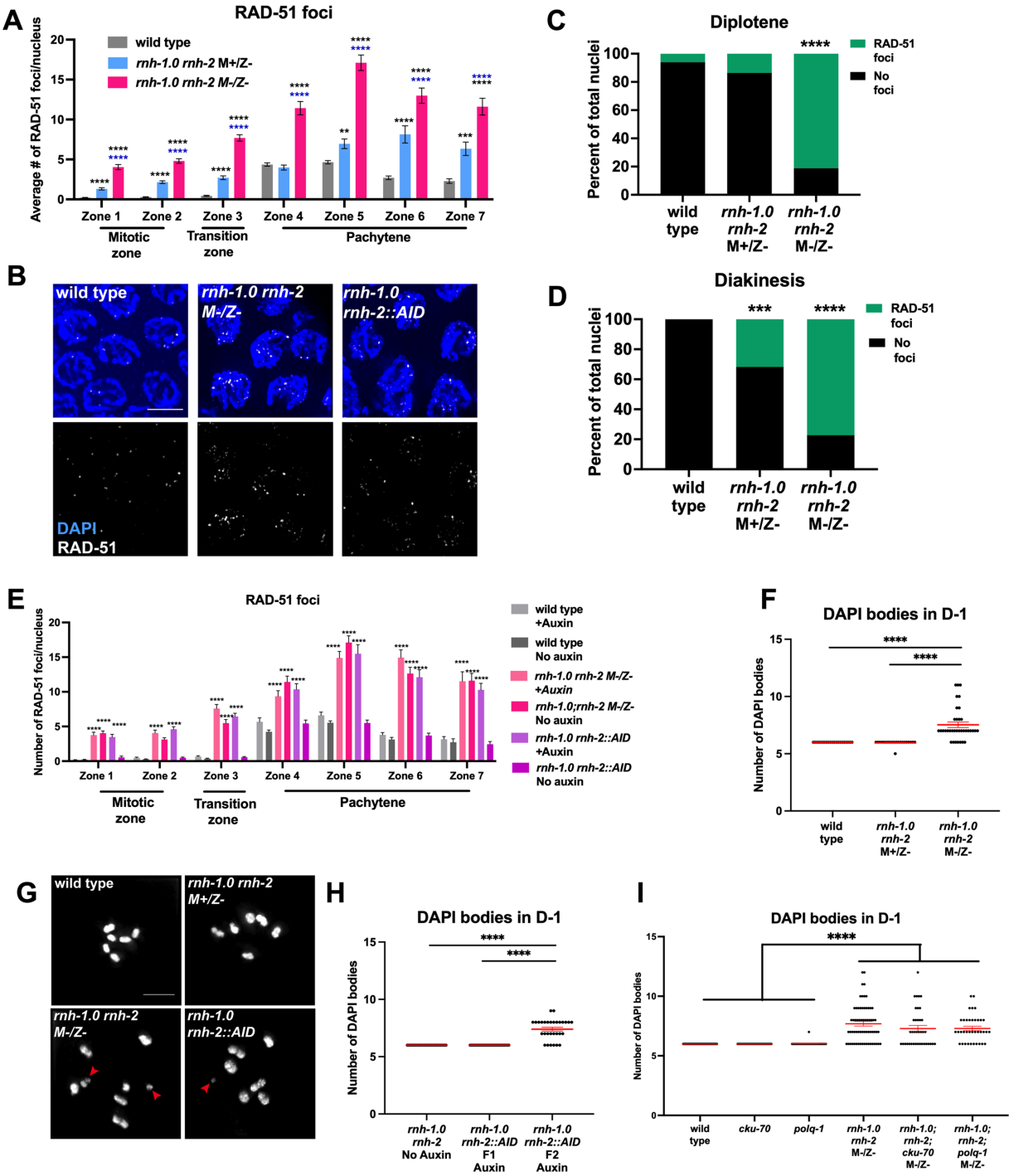

Figure 3. R-loops incur irreparable DSBs in the *C. elegans* germline. (**A**) Quantification of RAD-51 foci across the germline. X-axis indicates the zones along the gonad and the y-axis indicates average number of RAD-51 foci per nucleus. Error bars reflect mean with SEM. Asterisks indicate statistical significance calculated by Mann–Whitney *t*-test (****$P < 0.0001$, ***$P < 0.001$, **$P < 0.01$ and *$P < 0.05$). (**B**) Representative image of zone 5 nuclei in the indicated genotypes. Scale bar 4 μm. (**C**) Quantification of the number of diplotene nuclei with RAD-51 foci. Asterisks indicate statistical significance calculated by Fisher's exact *t*-test (****$P < 0.0001$, ***$P < 0.001$, **$P < 0.01$ and *$P < 0.05$). (**D**) Quantification of the number of diakinesis nuclei with RAD-51 foci. Asterisks indicate statistical significance calculated by Fisher's exact *t*-test (****$P < 0.0001$, ***$P < 0.001$, **$P < 0.01$ and *$P < 0.05$). (**E**) Quantification of RAD-51 foci across the germline. X-axis indicates the zones along the gonad and the y-axis indicates average number of RAD-51 foci per nucleus. Error bars reflect mean with SEM. Asterisks indicate statistical significance calculated by Mann–Whitney t-test (****$P < 0.0001$, ***$P < 0.001$, **$P < 0.01$ and *$P < 0.05$). Representative image of zone 5 above. Scale bar 4 μm. (**F**) Quantification of DAPI bodies in diakinesis nuclei in the indicated backgrounds and generations. Each data point reflects the number of DAPI bodies scored in one diakinesis nucleus. (**G**) Representative image of diakinesis oocytes for panel (F) and (H). Red arrows highlight chromosome fragments beyond bivalents. Scale bar 4 μm. (**H**) Quantification of DAPI bodies in diakinesis nuclei after exposure to auxin for two generations. Each data point reflects the number of DAPI bodies in one diakinesis nucleus. (**I**) Quantification of DAPI bodies in diakinesis nuclei of the indicated mutants. (F, H and I) Error bars reflect mean with SEM. Asterisks indicate statistical significance calculated by Mann–Whitney *t*-test (****$P < 0.0001$, ***$P < 0.001$, **$P < 0.01$ and *$P < 0.05$).

Irreparable breaks are mainly contributed by mitotic errors

The regulation of meiotic programmed DSBs catalyzed by the topoisomerase-like SPO-11 is integral to successful recombination and faithful chromosome segregation (7). We therefore sought to identify whether the irreparable DSBs observed in *rnh-1.0 rnh-2* germline oocytes were of meiotic origin or from events which precede the transition to meiosis. Using a *spo-11* null mutant background which lacks the ability to form programmed meiotic DSBs in tandem with the accumulation of R-loops in *rnh-1.0 rnh-2* mutant germlines, we separated mitotic damage phenotypes from those of SPO-11-induced breaks. RAD-51 focus quantification in *rnh-1.0 rnh-2; spo-11* germlines revealed a decrease in damage accumulation compared to *rnh-1.0 rnh-2* mutants (compare Figures 3A and 4A, Supplementary Figure S2A). However, relative to the *spo-11* single mutant control, triple mutants exhibited a significant increase in overall germline damage in both the M^+/Z^- and M^-/Z^- generations (Figure 4A and B), indicating that the majority of RAD-51 foci seen in *rnh-1.0 rnh-2* double mutants are of SPO-11-independent origins. Importantly however, the difference between the average number of RAD-51 foci per nucleus in *rnh-1.0 rnh-2* and *rnh-1.0 rnh-2; spo-11* germlines is comparable to the number of RAD-51 foci found in a wild-type background, indicating that DSBs in *rnh-1.0 rnh-2* germlines are a combination of SPO-11-induced meiotic breaks (as in wild type) and unrepaired mitotic breaks carried to meiotic prophase I.

Based on these findings, we sought to determine the origin of chromosome fragments found in *rnh-1.0 rnh-2* diakinesis oocytes. DAPI body counts in *rnh-1.0 rnh-2; spo-11* diakinesis, like *rnh-1.0 rnh-2*, displayed chromosome fragmentation events beyond the expected univalent observed in *spo-11* single mutants (Figure 4C and D). *rnh-1.0 rnh-2; spo-11* mutants also showed no evidence for crossover formation identified by the localization of the pro-crossover factor COSA-1 (Figure 4E, (31)). These data altogether indicate that the fragments observed formed independently of meiotic DSBs and that DNA damage generated from R-loops cannot generate crossovers that will substitute for SPO-11 induced DSBs.

Despite the accumulation of DNA damage in *rnh-1.0 rnh-2* M+/Z- (Figure 3A), they did not show chromosome fragments (Figure 3F), and removing meiotic DSBs (*spo-11* mutants) did not have an effect on DAPI body numbers (Supplementary Figure S3A). This data suggests that the appearance of fragments is correlated to the number of cell divisions in the absence of RNaseH activity. Since germ cells continue to divide throughout the lifetime of the adult, we tested whether 3-day old M^+/Z^-*rnh-1.0 rnh-2* adults show similar chromosome fragmentation to that of 1-day-old M^-/Z^-*rnh-1.0 rnh-2* adults. Indeed, aged *rnh-1.0 rnh*-2 M^+/Z^- worms exhibited an increase in both RAD-51 foci numbers and chromosomal fragmentation (Supplementary Figure S3B and C compared to Figure 4A and C M^+/Z^-), corroborating our earlier conclusion that an increased number of nuclear divisions enhances the phenotypic effects of R-loop accumulation. Thus, the increase in DAPI body counts in *rnh-1.0 rnh-2* mostly stems from mitotic DNA damage that accumulates with cellular divisions.

To confirm that DSBs induced in the pre-meiotic (mitotic) divisions, as opposed to meiotic prophase I, lead to chromosomal fragmentation, we exploited our auxin-inducible *rnh-2* allele *(rnh-1.0 rnh-2::AID)* to remove RNaseH activity specifically in the mitotic germline. First we determined that *rnh-1.0;rnh-2::AID* depletion for two generations leads to similar DNA fragmentation as observed in adult M^-/Z^- diakinesis (Figure 4F). Consistent with the RAD-51 foci counts (Figure 3E), RNaseH germline-specific depletion for two generations leads to an identical phenotype to ones observed in *rnh-1.0 rnh-2* M-Z-. To restrict RNaseH expression to mitotic/early meiotic cells of second-generation RNAseH-depleted worms, we recovered worms exposed to auxin on NGM for 60 h prior to analysis. This approach resulted in depletion of *rnh-2* in the PMT/TZ and allowed nuclei affected by this depletion to progress to diakinesis in the presence of RNAseH based on nuclei movement rate of ∼1 nuclear row per hour in the germline (32). Under these conditions, diakinesis chromosome fragments were again observed (Figure 4F). Moreover, auxin exposure for just 12 h was sufficient to lead to an increase in RAD-51 foci numbers in the PMT, and some TZ nuclei but not later in meiosis (Supplementary Figure S3D). Altogether, we conclude from these data that accumulated R-loops confer acute DNA damage mostly in the pre-meiotic stem cell niche which are not properly repaired in either mitotic or meiotic nuclei of the germline and manifest as chromosome fragments in the gametes.

The chromosomal fragments observed are likely caused by replication fork collapse and is expected to involve nucleases that identify the arrested fork and cleave it (33). Several structure-specific nucleases were shown to act in this context in mitotic cells and these nucleases act in double Holliday junction resolution in *C. elegans* meiosis (34–36). To assess the origin of mitotically-formed irreparable DSBs, we quantified diakinesis fragmentation events in *mus-81; rnh-1.0 rnh-2* M-/Z- mutants. The oocytes in this background reflect reduced chromosome fragments, indicating that MUS-81 likely contributes to the formation of irreparable DSBs in *rnh-1.0 rnh-2* M-/Z- germlines. Cleavage of R-loops by XPF and XPG was shown to contribute to DSB formation in other systems (37–40). Similar to our findings with *mus-81* mutants, analysis of *rnh-1.0 rnh-2* in conjunction with null mutations for *xpf-1* or *xpg-1* displayed reduced fragmentation events, suggesting that XPF-1 and XPG-1 also contribute to the formation of the irreparable breaks (Figure 4G). XPF-1 is also the only identified component in single strand annealing pathway (SSA) in *C. elegans* (41). The lack of increase in DAPI bodies in *rnh-1.0 rnh-2; xpf-1* mutants, also indicates that R-loop generated DSBs cannot be repaired by SSA.

DSBs caused by R-loops cannot properly activate mitotic cell cycle checkpoints but act synergistically with replication stress

DNA damage leads to cell cycle checkpoint activation, which can be temporary if DNA damage is repaired or terminal (i.e. senescence) if the DNA damage persists (42). The accumulation of resected DSBs (RAD-51 foci) in the mitotic region and the evidence that some of these DSBs

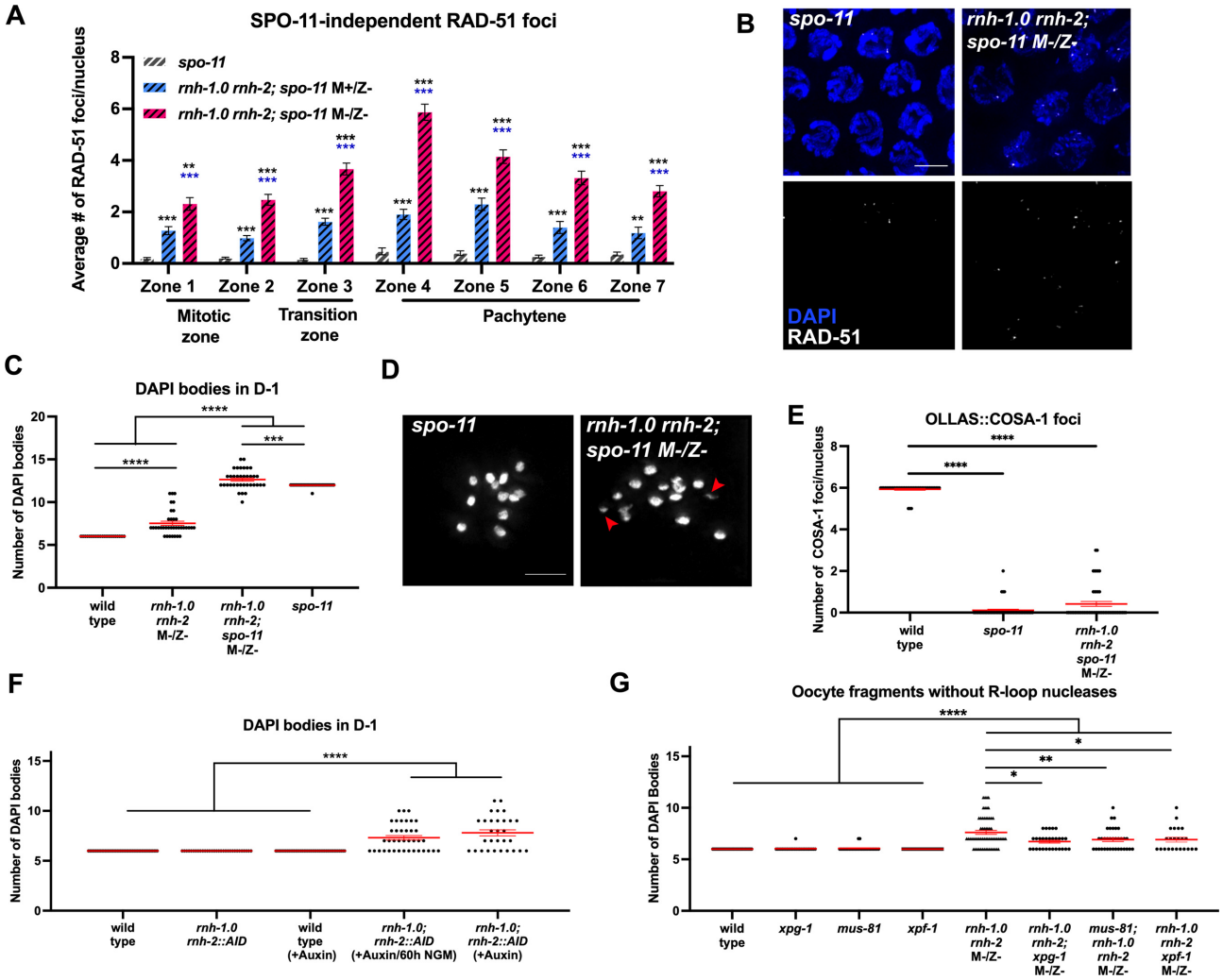

Figure 4. Irreparable breaks stem mainly from errors in the pre-meiotic stem cell niche. (**A**) Quantification of RAD-51 foci across the germline. X-axis indicates the zones along the gonad and the y-axis indicates average number of RAD-51 foci per nucleus. (**B**) Representative image of DSBs (RAD-51) in zone 4 nuclei in the indicated genotypes. Scale bar 4 μm. (**C**) Quantification of DAPI bodies in diakinesis nuclei in the indicated backgrounds and generations. Each data point reflects the number of DAPI bodies in one diakinesis nucleus. (**D**) Representative image of DAPI bodies in diakinesis. Scale bar 4 μm. Red arrows highlight chromosome fragments beyond univalents. (**E**) Quantification of COSA-1 foci in late pachytene nuclei in the indicated backgrounds and generations (**F**) Quantification of DAPI bodies in diakinesis nuclei in the indicated backgrounds and generations without auxin treatment, with auxin treatment for two generations (+Auxin), or auxin treatment for two generations with recovery to NGM for 60 h (+Auxin/60h NGM). Each data point reflects the number of DAPI bodies scored in one diakinesis nucleus. (**G**) Quantification of DAPI bodies in diakinesis nuclei in the indicated backgrounds. Each data point reflects the number of DAPI bodies in one diakinesis nucleus. All graphs: Error bars reflect mean with SEM. Asterisks indicate statistical significance calculated by Mann–Whitney *t*-test (****$P < 0.0001$, ***$P < 0.001$, **$P < 0.01$ and *$P < 0.05$).

are irreparable (chromosomal fragments) suggest activation of cell cycle arrest in our mutants. The activation of G1/S checkpoint should decrease S-phase entry, which can be identified by the percent of PCN-1 (PCNA)-positive nuclei (43). While ∼50% of wild-type nuclei were PCN-1-positive, only ∼30% of *rnh-1.0 rnh-2* M-/Z- nuclei had PCN-1 staining (Figure 5A and B). This suggests an effect of R-loops on the ability for these nuclei to enter or complete S-phase. To confirm this, we stained for the single-stranded binding protein RPA-2, which is essential for DNA replication and repair. RPA-2 appears as a nuclear 'haze' in replicating nuclei (18). Our analysis revealed a reduction from ∼50% nuclei with haze in wild type to ∼10% with haze in *rnh-1.0 rnh-2* M-/Z- (Figure 5C). To demonstrate that replicative defects revealed by PCN-1 and FLAG::RPA-2 staining are due to reduced replication and not just localization of replisome proteins, we tested for 5-ethynyl-2′-deoxyuridine (EdU) incorporation of *rnh-1.0 rnh-2* M-/Z- PMT nuclei after a 2-h chase (Figure 5D). EdU can only label nuclei that initiated replication in the 2-h window. In agreement with our earlier findings, we observed a reduction in the number of EdU-positive PMT nuclei of *rnh-1.0 rnh-2* M-/Z- germlines. Another indicator of cell cycle defects is an increase in nuclear volume. Nuclei continue to grow in volume in the presence of checkpoint activation, thus activation of the DNA damage checkpoint can be assessed by measurement of the nuclear diameter (44). Indeed, *rnh-1.0 rnh-2* mutants showed an increase in nuclear diameter compared to wild-type nu-

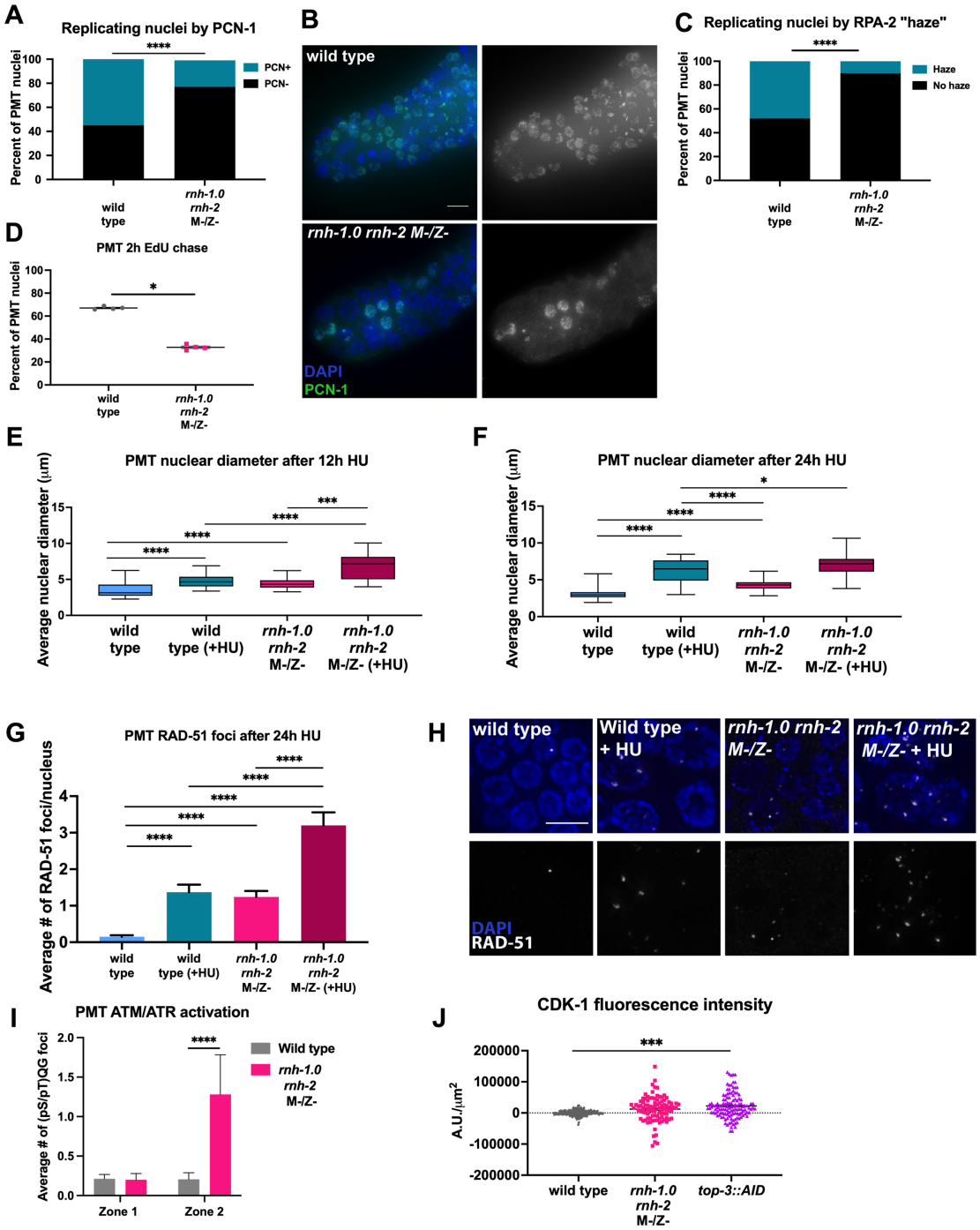

Figure 5. R-loops cause errors in cell cycle checkpoint activation and act synergistically with replication stress. (**A**) Quantification of the number of PMT nuclei with PCN-1 staining. Asterisks indicate statistical significance calculated by Fisher's exact *t*-test (****$P < 0.0001$, ***$P < 0.001$, **$P < 0.01$ and *$P < 0.05$). (**B**) Representative image of PCN-1 staining in (A). Scale bar 10 μm. (**C**) Quantification of the number of PMT nuclei with FLAG::RPA-2 staining appearing as a nuclear 'haze' (i.e. replicating nuclei). Asterisks indicate statistical significance calculated by Fisher's exact *t*-test (****$P < 0.0001$, ***$P < 0.001$, **$P < 0.01$ and *$P < 0.05$). (**D**) Quantification of the number of EdU-positive nuclei in the PMT after 2h EdU incorporation. Each data point reflects the percentage of EdU-positive nuclei per gonad. Error bars reflect mean with SEM. Asterisks indicate statistical significance calculated by Mann–Whitney t-test (****$P < 0.0001$, ***$P < 0.001$, **$P < 0.01$ and *$P < 0.05$). (**E**) Average nuclear diameter of PMT nuclei with (+HU) or without 12 h HU exposure. Asterisks indicate statistical significance calculated by Mann–Whitney t-test (****$P < 0.0001$, ***$P < 0.001$, **$P < 0.01$ and *$P < 0.05$). (**F**) As in (E) but after 24h HU exposure. (**G**) Quantification of the number of RAD-51 foci in PMT nuclei with (+HU) or without 24 h HU exposure in the indicated backgrounds. Error bars reflect mean with SEM. Asterisks indicate statistical significance calculated by Mann–Whitney t-test (****$P < 0.0001$, ***$P < 0.001$, **$P < 0.01$ and *$P < 0.05$). (**H**) Representative image of PMT nuclei from (E), (F), and (G). Scale bar 4 μm. (**I**) Quantification of the number of ATM/ATR foci in mitotic regions (zone 1 and zone 2) of the germline. Asterisks indicate statistical significance calculated by Mann–Whitney t-test (****$P < 0.0001$, ***$P < 0.001$, **$P < 0.01$ and *$P < 0.05$). (**J**) Measurement of CDK-1 fluorescence intensity in the indicated genotypes. Each data point represents the fluorescent signal of one nucleus corrected against the average background of the cytoplasm in that plane. Asterisks indicate statistical significance calculated by Mann–Whitney *t*-test (****$P < 0.0001$, ***$P < 0.001$, **$P < 0.01$ and *$P < 0.05$).

clei (Figure 5E and F). To determine whether this checkpoint response is sufficient to arrest G2/M-phase, we measured the length of the PMT and the number of nuclei in M-phase (Supplementary Figure S4A and B) in *rnh-1.0 rnh-2* germlines. We observed no increase in M-phase nuclei or decrease in the length of the PMT, phenotypes which would be expected in G2/M-phase-arrested germlines. These data altogether suggest that in the presence of R-loop-generated DSBs, cells do not enter and/or progress in a timely fashion into S-phase.

If the presence of DNA damage led to persistent cell cycle arrest, we would have expected that germline progression would be halted, leading to no meiotic entry. However, gonad length in the germline of *rnh-1.0 rnh-2* mutants only showed a small decrease with respect to the number of nuclear rows (84% of wild type) and nuclei numbers (79% of wild type) and not at all with respect for distance from the distal tip cell to the gonad's bend, indicating that the increased DNA damage may have slowed germline proliferation, but did not lead to proliferative arrest (Supplementary Figure S4C−G). We reasoned that although the S-phase checkpoint may be activated, this results only in a temporary cell cycle arrest. Indeed, when EdU was incorporated during longer chase times of 5 and 8 h (Supplementary Figure S4E and F), the observed defects were milder.

The lack of persistent arrest could be a measure of low levels of DSBs created by replication stress or a reflection of the type of DNA damage that caused the replication stress. Exposure to hydroxyurea (HU) results in increased nuclear volume as a byproduct of replication stress and DNA damage checkpoint activation (45). We therefore compared the nuclear expansion of *rnh-1.0 rnh-2* PMT nuclei to that of NGM- and HU-fed wild-type worms after short (12h) and long (24h) exposure (Figure 5E and F). Importantly, the level of DNA damage, as measured by RAD-51 foci, was comparable between untreated *rnh-1.0 rnh-2* nuclei and wild-type worms treated with HU (Figure 5G and H). Nuclear diameter measurements of these two conditions revealed a similar level of expansion in *rnh-1.0 rnh-2* PMT nuclei relative to the wild-type HU-treated PMT nuclei at the 12h timepoint, suggesting that some degree of checkpoint activation is achieved when R-loops are accumulated (Figure 5E). At the 24 h timepoint, average nuclear diameters further increased in the HU-treated control, compared to *rnh-1.0 rnh-2* mutants and wild type PMT nuclei (Figure 5F). Of note, *rnh-1.0 rnh-2* PMT nuclei expanded further when similarly treated with HU at both timepoints, indicating that HU stress acts independently of R-loop accumulation (Figure 5E and F). While RAD-51 foci numbers double in *rnh-1.0 rnh-2* mutants compared to wild type when both are exposed to HU for 24 h (Figure 5G), checkpoint activation is only slightly increased (Figure 5F). Treatment with HU for 24 h and recovery to NGM for 48 h allowed nuclei exposed to replication stress to progress into the late pachytene stage, where only a mild increase in damage was seen (Supplementary Figure S4G), compared to the effect in *rnh-1.0 rnh-2* mutants (Figure 3A and E). Therefore, despite similar DNA damage levels in the PMT to that of HU-treated nuclei, *rnh-1.0 rnh-2* PMT nuclei exhibit an attenuated DNA damage checkpoint response, leading to carryover of DNA damage into meiotic prophase I. Interestingly, a possible consequence to the checkpoint defects seen is sensitivity in the *rnh-1.0 rnh-2* M+/Z- generation to HU exposure (Supplementary Figure S4H). Altogether, these data suggest that the replicative stress induced by R-loops in *rnh-1.0 rnh-2* cycling nuclei attenuates the mitotic DNA damage checkpoint response, allowing for transmission of R-loop-generated DSBs into meiosis and conferring embryonic lethality.

To identify the causes of the defects in mitotic DNA damage-induced checkpoint in *rnh-1.0 rnh-2* germlines, we tested activation of the DNA damage signaling pathway. DNA damage sensing involves the activation of ATM/ATR through the phosphorylation of its targets that can be identifies by Phospho-ATM/ATR Substrate Motif [(pS/pT) QG] antibody. In mitotic cells, this activation is observed by elevation in the numbers of (pS/pT) QG foci. While no increase is observed in early mitotic regions of the germline (zone 1), in late mitotic regions of the germline (zone 2), *rnh-1.0 rnh-2* mutants exhibit an increase in (pS/pT) QG foci suggesting that ATM/ATR signaling is activated in response to R-loop accumulation (Figure 5I). Phosphorylation of ATM/ATR allows for phosphorylation of a tyrosine residue in the cell cycle effector CDK-1, inactivating it and causing cell cycle arrest (46,47). Depletion of topoisomerase 3 (*C. elegans* TOP-3) is associated with increased R-loop formation in higher eukaryotes (48). *top-3* mutants were previously shown to increase pCDK-1 levels in the PMT(49). We therefore compared pCDK-1 in *rnh-1.0 rnh-2* mutants relative to *top-3::AID* and wild-type worms. Our findings suggest that the phosphorylation of ATM/ATR in early germline regions successfully leads to an increase in pCDK-1 levels in these zones (Figure 5J). These data altogether are consistent with the attenuated cell cycle arrest observed in *rnh-1.0 rnh-2* mutants, and suggests that the attenuation stems from late (zone 2 versus 1) activation of ATM/ATR signaling.

DSBs caused by R-loops cannot properly activate apoptosis

Late pachytene nuclei in *C. elegans* can undergo two apoptotic processes; an EGL-1-dependent physiological apoptosis which culls the nuclei entering diplotene and is a normal, necessary part of worm meiosis and a DNA damage-linked, CEP-1-dependent apoptosis which removes irreparably damaged nuclei (9). Since apoptosis is used to clear damaged germline nuclei, it could provide a way to eliminate *rnh-1.0 rnh-2* nuclei which escaped the earlier mitotic checkpoint arrest and carried over replication-born RAD-51 foci to meiotic prophase I. Indeed, mutants that increase R-loops only on specific genes (*met-2; set-25*) activate apoptosis (14).

To directly test if apoptosis is executed, we quantified the number of CED-1::GFP-engulfed nuclei as a marker for nuclei undergoing apoptosis (Figure 6A). CED-1::GFP engulfment was similar in *rnh-1.0 rnh-2* M^-/Z^- mutants to wild-type levels, and much lower than in *syp-3* mutants that are known to accumulate RAD-51 foci in meiotic prophase I (50). This indicates that despite the accumulation of significant DSB formation due to R-loops, *rnh-1.0 rnh-2* mutants do not exhibit an increase in apoptosis. Acridine orange staining also revealed no change in apoptosis relative

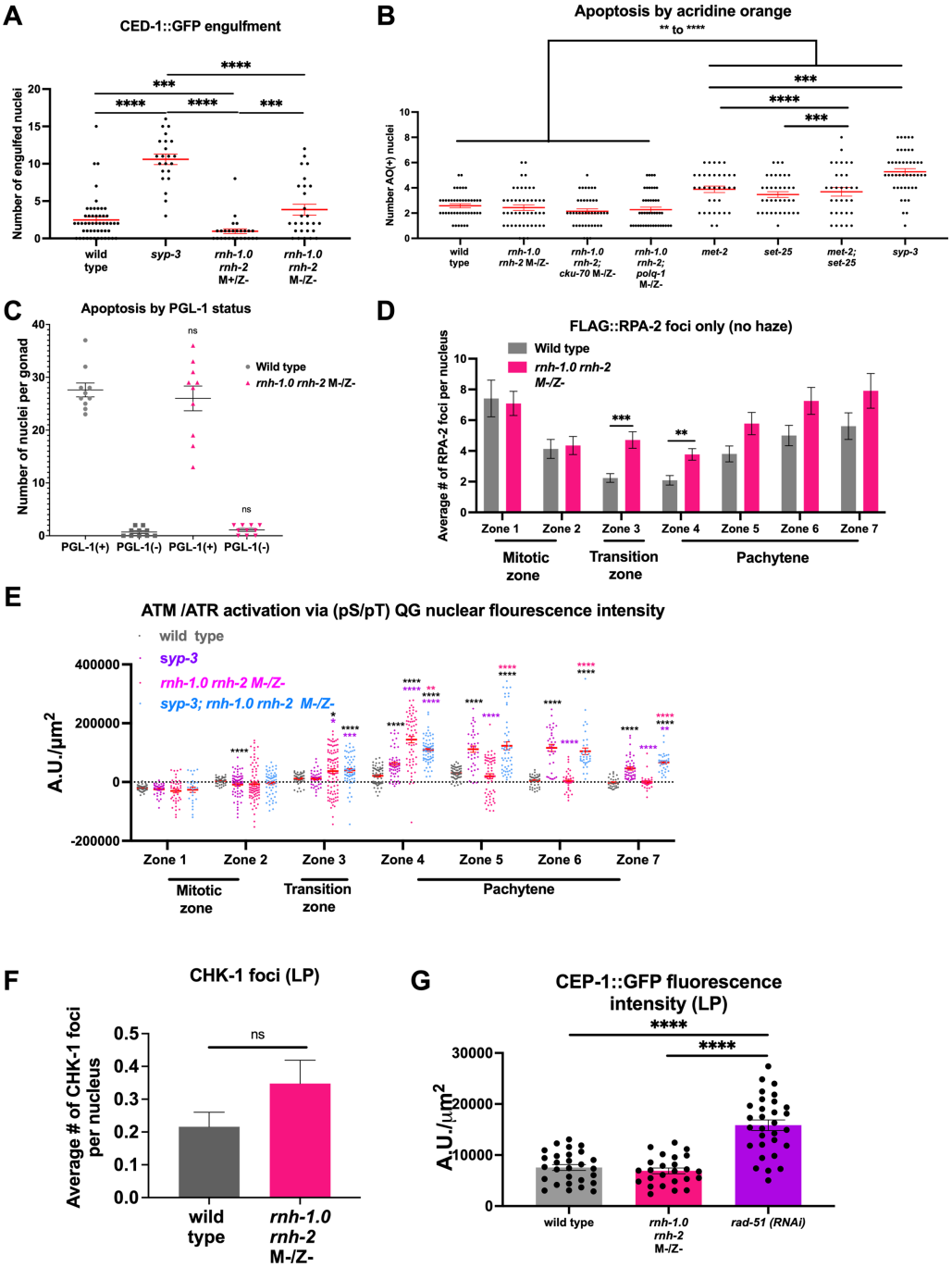

Figure 6. Irreparable damage is not channeled for apoptosis due to timing defects in ATM/ATR signaling. (**A**) Quantification of the number of pachytene nuclei with CED-1::GFP engulfment. Each data point reflects the number of nuclei in one gonad completely engulfed by CED-1::GFP. Black lines indicate median. Asterisks indicate statistical significance calculated by Mann–Whitney *t*-test (****$P < 0.0001$, ***$P < 0.001$, **$P < 0.01$ and *$P < 0.05$). (**B**) Quantification of the number of nuclei with acridine orange staining in the indicated backgrounds. Each data point reflects the number of acridine orange-positive nuclei in one gonad. Statistical significance calculated by Mann–Whitney *t*-test. (**C**) Quantification of the number of late pachytene nuclei with (+) or without (−) PGL-1 staining. Each data point reflects the number of nuclei within one gonad. Error bars reflect mean with SEM. Statistical comparisons drawn between quantifications of the same category (e.g. PGL-1(+) v. PGL-1(+)) by Mann–Whitney t-test. (**D**) Quantification of the number of FLAG::RPA-2 foci across the germline. X-axis denotes the zone of the germline and the y-axis reflects the average number of FLAG foci. Error bars reflect mean with SEM. Asterisks indicate statistical significance calculated by Mann–Whitney *t*-test (****$P < 0.0001$, ***$P < 0.001$, **$P < 0.01$ and *$P < 0.05$). (**E**) Measurements of ATM/ATR signaling. Fluorescence intensity of (pS/pT) QG signal across the gonad. X-axis denotes the zone of the germline and the y-axis denotes arbitrary fluorescent units per μm^2. Error bars reflect mean with SEM. Asterisks indicate statistical significance calculated by Mann–Whitney *t*-test (****$P < 0.0001$, ***$P < 0.001$, **$P < 0.01$ and *$P < 0.05$). Gray asterisks reflect significance compared to wild type, purple asterisks to *syp-3*, and pink asterisks to *rnh-1.0; rnh-2*. (**F**) Quantification of the number of CHK-1 foci in late pachytene nuclei. Error bars reflect mean with SEM. Statistical significance calculated by Mann–Whitney *t*-test. (**G**) Fluorescence intensity of CEP-1::GFP signal in late pachytene nuclei. Each data point reflects the fluorescence intensity of one LP nucleus with correction to the average background signal for that gonad. Error bars reflect mean with SEM. Asterisks indicate statistical significance calculated by Mann–Whitney *t*-test (****$P < 0.0001$, ***$P < 0.001$, **$P < 0.01$ and *$P < 0.05$).

to the wild type, an effect distinct from ones observed in mutants deficient in H3K9 methylation or DSB repair (Figure 6B and Supplementary Figure S5A). The P-granule marker PGL-1 is removed during DNA damage-induced apoptosis in *C. elegans*, and thus can be used to assess the levels of apoptosis (51). In agreement with CED-1::GFP and acridine orange staining, *rnh-1.0 rnh-2* exhibited no decrease in the number of PGL-1-positive nuclei, further evidencing a lack of apoptotic signaling in late pachytene (Figure 6C, Supplementary Figure S5B). Furthermore, assessment of RPA-4 localization, a marker for apoptotic signaling following replication stress (18), reveals no increase of FLAG::RPA-4 foci relative to wild type (Supplementary Figure S5C). Despite the inability to activate apoptosis, nuclei with irreparable DSBs can delay their pachytene entry, as the number of nuclei per nuclear row in TZ was increased (Supplementary Figure S5D and E), while the number of nuclei per row in pachytene regions of the germline was reduced (Supplementary Figure S5F and G). Lack of activation of apoptosis may stem from the repair of DSBs by non-homologous end joining (NHEJ), as observed in *top-3::AID* mutants (49). However, *cku-70* null mutants had no effect on apoptosis in *rnh-1.0 rnh-2* mutants or the number of chromosomal fragments in oocytes (Figure 6B and D, respectively). These results also suggest that NHEJ does not contribute to repair of R-loop-induced DSBs, which is supported by the lack of chromosomal fusions in these mutants (Figure 3F and H).

Taking into account our observation that cell cycle arrest in the mitotic region is stemming from attenuation of the DNA damage checkpoint, we reasoned that those apoptotic effects are also associated with reduced or eliminated DNA damage signaling. Similar to mitotic cell cycle arrest, meiotic apoptosis requires ATM (ATM-1) and ATR (ATL-1) activation in pachytene (46). RPA is known to mediate ATR activation and serves an R-loop sensor (52). Indeed, RPA foci numbers are increased in non-replicative germline nuclei of *rnh-1.0 rnh-2* M-/Z- mutants compared to wild type as they enter meiosis (zone 3 and 4, Figure 6D), but are not significantly increased in pachytene. ATM/ATR activation in pachytene is indicated by an increase in nuclear staining of (pS/pT) QG antibody (Figures 6E and Figure 5SG). Despite high levels of persisting DNA damage (Figure 3A) we observed no increase in foci numbers or nuclear localization of (pS/pT) QG in mid- to late pachytene, when apoptosis is activated (zone 5–7, Figure 6E). We compared our measurements to that of *syp-3* mutants which lack a fully assembled synaptonemal complex necessary for proper meiotic DSB repair and which are able to activate ATM/ATR leading to apoptosis (50). We also compared our measurements in the late pachytene region to wild-type worms treated with 50 μM etoposide, which has been shown to induce ATM/ATR signaling previously, with corroborating results (Supplementary Figure S5H). This comparison shows that while ATM/ATR activation occurs in early pachytene of *rnh-1.0 rnh-2* mutants, it is rapidly and strikingly lost at the same time that *syp-3* mutants experience an increase in p(S/pT) QG localization (Figure 6E). Most importantly, removal of *syp-3* from *rnh-1.0 rnh-2* mutants can lead to ATM/ATR target activation, indicating that *rnh-1.0 rnh-2* mutants are capable of DNA damage signaling from DSBs that are not R-loop driven (Figure 6E and Supplementary Figure S5I).

We further tested the activation of the downstream target CHK-1 in late pachytene. In agreement with this result, unlike what is seen in PMT nuclei, the number of CHK-1 foci does not significantly increase in *rnh-1.0 rnh-2* M-/Z- pachytene (Figure 6F). Similarly, and unlike in mutants deficient in DSB repair [*rad-51(RNAi)*], apoptotic signaling, was hindered in *rnh-1.0 rnh-2* mutants, as expected from loss of ATM/ATR activation in pachytene (Figure 6G, by proxy of CEP-1, the *C. elegans* p53 ortholog, (53)). This observation, taken together with accumulation of RAD-51 foci and DNA fragmentation in *rnh-1.0 rnh-2* mutants, indicates that R-loop-induced irreparable DSBs cannot properly activate DNA damage checkpoints, which may stem from premature RPA removal. Avoiding apoptosis may explain how nuclei with irreparable damage are found in oocytes.

DISCUSSION

The balance between pathological and physiologically-required R-loops is key to ensuring the success of normal cellular processes without detrimental effects (1,2). Here we have identified RNaseH1 and H2 to be required for regulating this balance in the meiotic environment and have described the consequences of R-loop accumulation on viable gamete formation in the *C. elegans* germline. We have found that the RNaseH1 and H2 enzymes, which have been extensively reported as key regulatory elements in the control of R-loop accumulation, are present within the *C. elegans* germline. When RNaseH1 and H2 are absent, we similarly find that DNA–RNA hybrids accumulate in the germline specifically at highly-expressed loci. The overabundance of R-loops in this background is further accompanied by a dramatic elevation in DSB formation (fragments) and perhaps most intriguingly, an inability to properly recognize and respond to R-loop-induced DSBs. The ability to evade late activation of ATM/ATR may explain the observed lack of CEP-1 localization and wild-type levels of apoptosis despite extensive damage. As a result, chromosomal fragments are observed in the oocytes of *rnh-1.0 rnh-2* M-/Z- worms and the continued division of nuclei containing R-loop-induced damage appears to cause generational sterility and genome instability in *C. elegans*. It is formally possible that perturbing RNAseH function has phenotypic consequences beyond the effect on genomic stability. For example, R-loops are required for the regulation of transcription termination and RNA−DNA hybrid removal is essential for Okazaki fragment maturation. These direct effects were not examined in this study and likely have a minor contribution to the phenotype due to the redundancy described in other systems (54).

While the consequences of R-loop formation have been described previously in other systems and contexts, their effects in the context of the meiotic cellular environment have been poorly studied. Moreover, studies using different models for R-loop accumulation led to different conclusions of their role in meiosis. For instance, mutants that lead to the accumulation of R-loops via their effects on mRNP biogenesis (THO complex) exhibit very severe effects on meiosis (55), while mutants that affect chromatin modifications

(*met-2* and *set-25*) and accumulate R-loops as a result, have a more limited effect (14). For example, yeast THO complex mutants' spore viability is almost halved, while spore viability is not compromised to the same levels in RNaseH mutants (12,56). Impairment of the THO complex in mouse and *C. elegans* models results in even more profound effects on meiosis, leading to meiotic failures (55). Alternatively, *C. elegans met-2; set-25* mutants complete prophase I and produce oocytes, with some temperature-dependent reduction in fertility (14). These effects together suggest R-loops impair meiosis, however it is likely that the effects of perturbing the THO complex are more notable due to the combined role of the THO complex in R-loop removal and mRNP biogenesis.

The manner by which R-loops perturb meiosis is not fully understood. However, it is clear that R-loops lead to replication stress in the pre-meiotic divisions, leading to DNA damage accumulation and transmission of DSBs to meiotic cells. Prior to our studies, it was reasonable to propose that R-loop-generated DSBs are dealt with like other forms of DNA damage: meiotic cells can either repair high levels of DNA damage or use apoptosis to clear damaged cells that cannot be properly repaired. When chromosome integrity was examined in *met-2; set-25* mutants, no effects on chromosome integrity, crossovers or segregation were observed (14). In yeast, excessive or reduced R-loops were linked to reduced crossovers (16). However, no such effects were observed in other systems, including ours. In this regard, our identification of DNA fragmentation alongside chiasmata is intriguing, suggesting that DSB formation following R-loop-generated replication stress is not being properly repaired by the meiotic repair machineries in the *C. elegans* germline.

R-loops are associated with genome instability that is propagated to daughter cells following subsequent cell divisions (56,57). The propagation of genomic instability is thought to be the outcome of error-prone repair of R-loop-generated DSBs. While propagation of large-scale chromosomal rearrangements (i.e. deletions, duplication, and translocations) was documented in budding yeast, irreparable DSBs lead to cell cycle arrest and therefore are not transmitted to daughter cells (57). Our studies point to a different picture in *C. elegans* that may be translatable to metazoan meiosis: R-loops contribute to chromosomal fragmentation that is inherited through cell divisions; unlike irreparable damage in mitotic cells, germline irreparable DSBs evade detection and are carried over to gametes. It is particularly peculiar that irreparable DSBs are found in the germline, a tissue that is accustomed to a multitude of programmed DSBs [up to 500 DSBs/nucleus depending on the organism (6)]. Germline DSBs are preferentially repaired by homologous recombination, and when this pathway is blocked or impaired, NHEJ and TMEJ and SSA can be used for DSB repair leading to chromosomal fusions [e.g. (10,11,30,41)]. We observed no such fusions in our mutants, indicating that all repair pathways are inhibited when R-loops accumulate on a global scale. Although we do not yet know what feature of R-loops generates irreparable DSBs, we have shown that structure-specific nucleases (XPF-1, MUS-81 and XPF-1) contribute to fragmentation. These findings suggest that replication–transcription conflict leads to fork cleavage and release of a chromosomal fragment. The accumulation of RAD-51 foci indicates that resection takes place, which may explain why alternative repair pathways are not involved in repair in this context. It is possible that the presence of R-loops prevents double Holliday junction formation, such that DSB repair is blocked following RAD-51 filament formation as proposed in yeast (58). This may explain why in the absence of meiotic DSBs, R-loop- generated DSBs cannot support crossover formation (by DAPI body or COSA-1 analysis). It is also formally possible that some DSBs are not processed (cannot be identified by RAD-51) and these DSBs are more likely to avoid repair. However, this model cannot easily explain why these DSBs are not repaired by alternative repair pathways (cNHEJ, TMEJ, SSA). It is important to note that RAD-51 may label different intermediates that are not processed DSBs, such as regressed forks (59). However, these are likely to be observed in the mitotic and not meiotic region of the germline.

When the germline stem cell niche nuclei are challenged by excessive DSBs, these DSBs elicit cell cycle arrest (60). In the *C. elegans* germline DNA damage leads to ATM-1 and ATL-1(ATR homolog) signaling and cell cycle arrest in the mitotic zone(46). The effect of R-loops on these germline events has not been examined before and here we provide evidence that R-loop-induced DSBs lead to attenuated cell cycle arrest compared to DSBs invoked by other forms of replication stress. These findings are distinct from what is found in yeast (57), suggesting that the metazoan cell cycle may not respond the same way to R-loop-generated DNA damage. The delay in accumulation of (pS/pT) QG foci (Figure 5D) may indicate that these defects stem from early events in DNA damage signaling, that are common with apoptotic signaling (see below).

It is well established that accumulation of DNA damage leads to an increase in germline apoptosis (60,61). This allows the removal of damaged oocytes at late pachytene, such that even under high levels of DNA damage, oocyte quality is partially impaired (60). *C. elegans* apoptosis is governed by a conserved signaling cascade that leads to DNA fragmentation, nuclear engulfment, and removal (62). Despite the high levels of DNA damage, manifested by accumulation of RAD-51 foci, the apoptotic program is not executed in *rnh-1.0 rnh-2* mutants. As observed in the mitotic region, these defects are related to the attenuation of ATM/ATR signaling. The magnitude of the defective ATM/ATR signaling in pachytene compared to the mitotic region correlates with more severe defects on apoptosis (late pachytene) vs. cell cycle arrest (mitotic region). This indicates, again, that R-loop-mediated DNA damage can avoid detection in the germline, leading to its propagation in oocytes. The inability to activate DNA damage signaling is not due to indirect effects perturbing the signaling machinery, as *rnh-1.0 rnh-2* mutants can respond to meiotic DSB accumulation (*syp-3* mutants) and activate ATM/ATR signaling. Interestingly, *met-2* pathway mutants that accumulate R-loops, specifically on untranscribed regions, are able to activate apoptosis (14,63). Altogether, this suggests that it is not the R-loops or R-loop-generated DSBs *per se* that attenuate ATM/ATR signaling, but that it is a context-specific effect; R-loops at specific genomic locations are responsible for this attenuation. What feature of R-loops and genomic

context prevents the activation of ATM/ATR signaling is the target of future studies.

DATA AVAILABILITY

Strains are available upon request. The authors state that all data necessary for confirming the conclusions presented in the article are represented fully within the article.

SUPPLEMENTARY DATA

Supplementary Data are available at NAR Online.

ACKNOWLEDGEMENTS

Some strains and clones were kindly provided by the *Caenorhabditis* Genetics Center, which is funded by the National Institutes of Health (NIH) Office of Research Infrastructure Programs (P40 OD-010440), and the *C. elegans* Reverse Genetics Core Facility at the University of British Columbia, which is part of the International *C. elegans* Gene Knockout Consortium. We thank the National Bioresource Project for the Experimental Animal 'Nematode C. elegans', Japan for providing alleles for this study. We thank Matthew Michael for the PCN-1 antibody and Patrick DiMario for the Fibrillarin antibody. We thank Tina Tootle and Nicola Silva for helpful discussions and the Smolikove lab members for reading the manuscript.

FUNDING

National Science Foundation [2027955]. Funding for open access charge: NSF [2027955].
Conflict of interest statement. None declared.

REFERENCES

1. Allison,D.F. and Wang,G.G. (2019) R-loops: formation, function, and relevance to cell stress. *Cell Stress*, **3**, 38–46.
2. Garcia-Muse,T. and Aguilera,A. (2019) R Loops: from physiological to pathological roles. *Cell*, **179**, 604–618.
3. Zhao,H., Zhu,M., Limbo,O. and Russell,P. (2018) RNase h eliminates R-loops that disrupt DNA replication but is nonessential for efficient DSB repair. *EMBO Rep.*, **19**, e45335.
4. Cerritelli,S.M. and Crouch,R.J. (2009) Ribonuclease H: the enzymes in eukaryotes. *FEBS J.*, **276**, 1494–1505.
5. Keskin,H., Shen,Y., Huang,F., Patel,M., Yang,T., Ashley,K., Mazin,A.V. and Storici,F. (2014) Transcript-RNA-templated DNA recombination and repair. *Nature Publishing Group*, **515**, 436–439.
6. Martinez-Perez,E. and Colaiácovo,M.P. (2009) Distribution of meiotic recombination events: talking to your neighbors. *Curr. Opin. Genet. Dev.*, **19**, 105–112.
7. Robert,T., Vrielynck,N., Mézard,C., de Massy,B. and Grelon,M. (2016) A new light on the meiotic DSB catalytic complex. *Semin. Cell Dev. Biol.*, **54**, 165–176.
8. Szekvolgyi,L., Ohta,K. and Nicolas,A. (2015) Initiation of meiotic homologous recombination: flexibility, impact of histone modifications, and chromatin remodeling. *Cold Spring Harb. Perspect. Biol.*, **7**, a016527.
9. Gartner,A. and Engebrecht,J. (2022) DNA repair, recombination, and damage signaling. *Genetics*, **220**, iyab178.
10. Martin,J.S., Winkelmann,N., Petalcorin,M.I.R., McIlwraith,M.J. and Boulton,S.J. (2005) RAD-51-dependent and -independent roles of a *Caenorhabditis elegans* BRCA2-related protein during DNA double-strand break repair. *Mol. Cell. Biol.*, **25**, 3127–3139.
11. Yin,Y. and Smolikove,S. (2013) Impaired resection of meiotic double-strand breaks channels repair to nonhomologous end joining in *Caenorhabditis elegans*. *Mol. Cell. Biol.*, **33**, 2732–2747.
12. Castellano-Pozo,M., Garcia-Muse,T. and Aguilera,A. (2012) R-loops cause replication impairment and genome instability during meiosis. *EMBO Rep.*, **13**, 923–929.
13. Becherel,O.J., Yeo,A.J., Stellati,A., Heng,E.Y.H., Luff,J., Suraweera,A.M., Woods,R., Fleming,J., Carrie,D., McKinney,K. *et al.* (2013) Senataxin plays an essential role with DNA damage response proteins in meiotic recombination and gene silencing. *PLos Genet.*, **9**, e1003435.
14. Zeller,P., Padeken,J., van Schendel,R., Kalck,V., Tijsterman,M. and Gasser,S.M. (2016) Histone H3K9 methylation is dispensable for *Caenorhabditis elegans* development but suppresses RNA:DNA hybrid-associated repeat instability. *Nat. Genet.*, **48**, 1385–1395.
15. Padeken,J., Zeller,P., Towbin,B., Katic,I., Kalck,V., Methot,S.P. and Gasser,S.M. (2019) Synergistic lethality between BRCA1 and H3K9me2 loss reflects satellite derepression. *Genes Dev.*, **33**, 436–451.
16. Yang,X., Zhai,B., Wang,S., Kong,X., Tan,Y., Liu,L., Yang,X., Tan,T., Zhang,S. and Zhang,L. (2021) RNA-DNA hybrids regulate meiotic recombination. *Cell Rep.*, **37**, 110097.
17. Zimmer,A.D. and Koshland,D. (2016) Differential roles of the RNases h in preventing chromosome instability. *Proc. Natl. Acad. Sci. U.S.A.*, **113**, 12220–12225.
18. Hefel,A., Honda,M., Cronin,N., Harrell,K., Patel,P., Spies,M. and Smolikove,S. (2021) RPA complexes in *Caenorhabditis elegans* meiosis; unique roles in replication, meiotic recombination and apoptosis. *Nucleic Acids Res.*, **49**, 2005–2026.
19. Janisiw,E., Raices,M., Balmir,F., Paulin,L.F., Baudrimont,A., von Haeseler,A., Yanowitz,J.L., Jantsch,V. and Silva,N. (2020) Poly(ADP-ribose) glycohydrolase coordinates meiotic DNA double-strand break induction and repair independent of its catalytic activity. *Nat. Commun.*, **11**, 4869.
20. Michael,W.M. (2016) Cyclin CYB-3 controls both S-phase and mitosis and is asymmetrically distributed in the early c. elegans embryo. *Development*, **143**, 3119–3127.
21. Colaiácovo,M.P., MacQueen,A.J., Martinez-Perez,E., McDonald,K., Adamo,A., La Volpe,A. and Villeneuve,A.M. (2003) Synaptonemal complex assembly in c. elegans is dispensable for loading strand-exchange proteins but critical for proper completion of recombination. *Dev. Cell*, **5**, 463–474.
22. Alpi,A., Pasierbek,P., Gartner,A. and Loidl,J. (2003) Genetic and cytological characterization of the recombination protein RAD-51 in *Caenorhabditis elegans*. *Chromosoma*, **112**, 6–16.
23. Gartner,A., MacQueen,A.J. and Villeneuve,A.M. (2004) Methods for analyzing checkpoint responses in *Caenorhabditis elegans*. *Methods Mol. Biol.*, **280**, 257–274.
24. Arudchandran,A., Cerritelli,S.M., Bowen,N.J., Chen,X., Krause,M.W. and Crouch,R.J. (2002) Multiple ribonuclease H-encoding genes in the *Caenorhabditis elegans* genome contrasts with the two typical ribonuclease H-encoding genes in the human genome. *Mol. Biol. Evol.*, **19**, 1910–1919.
25. Kochiwa,H., Itaya,M., Tomita,M. and Kanai,A. (2006) Stage-specific expression of *Caenorhabditis elegans* ribonuclease H1 enzymes with different substrate specificities and bivalent cation requirements. *FEBS J.*, **273**, 420–429.
26. Hsu,J.Y., Sun,Z.W., Li,X.-Y., Reuben,M., Tatchell,K., Bishop,D.K., Grushcow,J.M., Brame,C.J., Caldwell,J.A., Hunt,D.F. *et al.* (2000) Mitotic phosphorylation of histone H3 is governed by Ipl1/aurora kinase and glc7/pp1 phosphatase in budding yeast and nematodes. *Cell*, **102**, 279–291.
27. St Germain,C., Zhao,H. and Barlow,J.H. (2021) Transcription-replication collisions - a series of unfortunate events. *Biomolecules*, **11**, 1249.
28. Tzur,Y.B., Winter,E., Gao,J., Hashimshony,T., Yanai,I. and Colaiácovo,M.P. (2018) Spatiotemporal gene expression analysis of the *Caenorhabditis elegans* germline uncovers a syncytial expression switch. *Genetics*, **210**, 587–605.
29. Zhang,L., Ward,J.D., Cheng,Z. and Dernburg,A.F. (2015) The auxin-inducible degradation (AID) system enables versatile conditional protein depletion in c. elegans. *Development*, **142**, 4374–4384.
30. Macaisne,N., Kessler,Z. and Yanowitz,J.L. (2018) Meiotic double-strand break proteins influence repair pathway utilization. *Genetics*, **210**, 843–856.

31. Yokoo,R., Zawadzki,K.A., Nabeshima,K., Drake,M., Arur,S. and Villeneuve,A.M. (2012) COSA-1 reveals robust homeostasis and separable licensing and reinforcement steps governing meiotic crossovers. *Cell*, **149**, 75–87.
32. Jaramillo-Lambert,A., Ellefson,M., Villeneuve,A.M. and Engebrecht,J. (2007) Differential timing of s phases, x chromosome replication, and meiotic prophase in the c. elegans germ line. *Dev. Biol.*, **308**, 206–221.
33. Liao,H., Ji,F., Helleday,T. and Ying,S. (2018) Mechanisms for stalled replication fork stabilization: new targets for synthetic lethality strategies in cancer treatments. *EMBO Rep.*, **19**, e46263.
34. Agostinho,A., Meier,B., Sonneville,R., Jagut,M., Woglar,A., Blow,J., Jantsch,V. and Gartner,A. (2013) Combinatorial regulation of meiotic holliday junction resolution in c. elegans by HIM-6 (BLM) helicase, SLX-4, and the SLX-1, MUS-81 and XPF-1 nucleases. *PLos Genet.*, **9**, e1003591.
35. Saito,T.T., Lui,D.Y., Kim,H.-M., Meyer,K. and Colaiácovo,M.P. (2013) Interplay between structure-specific endonucleases for crossover control during *Caenorhabditis elegans* meiosis. *PLoS Genet.*, **9**, e1003586.
36. O'Neil,N.J., Martin,J.S., Youds,J.L., Ward,J.D., Petalcorin,M.I.R., Rose,A.M. and Boulton,S.J. (2013) Joint molecule resolution requires the redundant activities of MUS-81 and XPF-1 during *Caenorhabditis elegans* meiosis. *PLos Genet.*, **9**, e1003582.
37. Sollier,J., Stork,C.T., Garcia-Rubio,M.L., Paulsen,R.D., Aguilera,A. and Cimprich,K.A. (2014) Transcription-coupled nucleotide excision repair factors promote R-loop-induced genome instability. *Mol. Cell*, **56**, 777–785.
38. Yasuhara,T., Kato,R., Hagiwara,Y., Shiotani,B., Yamauchi,M., Nakada,S., Shibata,A. and Miyagawa,K. (2018) Human rad52 promotes XPG-mediated R-loop processing to initiate transcription-associated homologous recombination repair. *Cell*, **175**, 558–570.
39. Cristini,A., Ricci,G., Britton,S., Salimbeni,S., Huang,S.N., Marinello,J., Calsou,P., Pommier,Y., Favre,G., Capranico,G. *et al.* (2019) Dual processing of R-Loops and topoisomerase i induces transcription-dependent DNA double-strand breaks. *Cell Rep.*, **28**, 3167–3181.
40. Goulielmaki,E., Tsekrekou,M., Batsiotos,N., Ascensao-Ferreira,M., Ledaki,E., Stratigi,K., Chatzinikolaou,G., Topalis,P., Kosteas,T., Altmuller,J. *et al.* (2021) The splicing factor XAB2 interacts with ERCC1-XPF and XPG for R-loop processing. *Nat. Commun.*, **12**, 3153.
41. Bae,W., Hong,S., Park,M.S., Jeong,H.-K., Lee,M.-H. and Koo,H.-S. (2019) Single-strand annealing mediates the conservative repair of double-strand DNA breaks in homologous recombination-defective germ cells of *Caenorhabditis elegans*. *DNA Repair (Amst.)*, **75**, 18–28.
42. Blackford,A.N. and Stucki,M. (2020) How cells respond to DNA breaks in mitosis. *Trends Biochem. Sci*, **45**, 321–331.
43. Michael,W.M. (2016) Cyclin CYB-3 controls both S-phase and mitosis and is asymmetrically distributed in the early c. elegans embryo. *Development*, **143**, 3119–3127.
44. Craig,A.L., Moser,S.C., Bailly,A.P. and Gartner,A. (2012) In: *Methods for Studying the DNA Damage Response in the Caenorhabdatis elegans Germ Line*. 2nd edn. Elsevier Inc.
45. MacQueen,A.J. and Villeneuve,A.M. (2001) Nuclear reorganization and homologous chromosome pairing during meiotic prophase require c. elegans chk-2. *Genes & Development*, **15**, 1674–1687.
46. Garcia-Muse,T. and Boulton,S.J. (2005) Distinct modes of ATR activation after replication stress and DNA double-strand breaks in *Caenorhabditis elegans*. *EMBO J.*, **24**, 4345–4355.
47. Kalogeropoulos,N., Christoforou,C., Green,A.J., Gill,S. and Ashcroft,N.R. (2004) chk-1 is an essential gene and is required for an S-M checkpoint during early embryogenesis. *Cell Cycle*, **3**, 1196–1200.
48. Zhang,T., Wallis,M., Petrovic,V., Challis,J., Kalitsis,P. and Hudson,D.F. (2019) Loss of TOP3B leads to increased R-loop formation and genome instability. *Open Biol*, **9**, 190222.
49. Dello Stritto,M.R., Bauer,B., Barraud,P. and Jantsch,V. (2021) DNA topoisomerase 3 is required for efficient germ cell quality control. *J. Cell Biol.*, **220**, e202012057.
50. Smolikov,S., Eizinger,A., Hurlburt,A., Rogers,E., Villeneuve,A.M. and Colaiacovo,M.P. (2007) Synapsis-Defective mutants reveal a correlation between chromosome conformation and the mode of double-strand break repair during *Caenorhabditis elegans* meiosis. *Genetics*, **176**, 2027–2033.
51. Min,H., Shim,Y.H. and Kawasaki,I. (2016) Loss of PGL-1 and PGL-3, members of a family of constitutive germ-granule components, promotes germline apoptosis in c. elegans. *J. Cell Sci.*, **129**, 341–353.
52. Nguyen,H.D., Yadav,T., Giri,S., Saez,B., Graubert,T.A. and Zou,L. (2017) Functions of replication protein a as a sensor of r loops and a regulator of RNaseH1. *Mol. Cell*, **65**, 832–847.
53. Schumacher,B., Hofmann,K., Boulton,S.J. and Gartner,A. (2001) The c. elegans homolog of the p53 tumor suppressor is required for DNA damage-induced apoptosis. **11**, 1722–1727.
54. Kao,H.I. and Bambara,R.A. (2003) The protein components and mechanism of eukaryotic okazaki fragment maturation. *Crit. Rev. Biochem. Mol. Biol.*, **38**, 433–452.
55. Castellano-Pozo,M., Garcia-Muse,T. and Aguilera,A. (2012) The *Caenorhabditis elegans* THO complex is required for the mitotic cell cycle and development. *PLoS One*, **7**, e52447.
56. Huertas,P. and Aguilera,A. (2003) Cotranscriptionally formed DNA:RNA hybrids mediate transcription elongation impairment and transcription-associated recombination. *Mol. Cell*, **12**, 711–721.
57. Costantino,L. and Koshland,D. (2018) Genome-wide map of R-Loop-Induced damage reveals how a subset of R-Loops contributes to genomic instability. *Mol. Cell*, **71**, 487–497.
58. Amon,J.D. and Koshland,D. (2016) RNase h enables efficient repair of R-loop induced DNA damage. *Elife*, **5**, e20533.
59. Wassing,I.E. and Esashi,F. (2021) RAD51: beyond the break. *Semin. Cell Dev. Biol.*, **113**, 38–46.
60. Gartner,A., Milstein,S., Ahmed,S., Hodgkin,J. and Hengartner,M.O. (2000) A conserved checkpoint pathway mediates DNA damage–induced apoptosis and cell cycle arrest in c. elegans. *Mol. Cell*, **5**, 435–443.
61. Gumienny,T.L., Lambie,E., Hartwieg,E., Horvitz,H.R. and Hengartner,M.O. (1999) Genetic control of programmed cell death in the *Caenorhabditis elegans* hermaphrodite germline. *Development*, **126**, 1011–1022.
62. Gartner,A., Boag,P.R. and Blackwell,T.K. (2008) In: *Germline Survival and Apoptosis*. WormBook, 1–20.
63. Yang,B., Xu,X., Russell,L., Sullenberger,M.T., Yanowitz,J.L. and Maine,E.M. (2019) A DNA repair protein and histone methyltransferase interact to promote genome stability in the Caenorhabditis elegans germ line. *PLoS Genetics*, **15**, e1007992.